Article

Cell Host & Microbe

Impact of SARS-CoV-2 ORF6 and its variant polymorphisms on host responses and viral pathogenesis

Graphical abstract

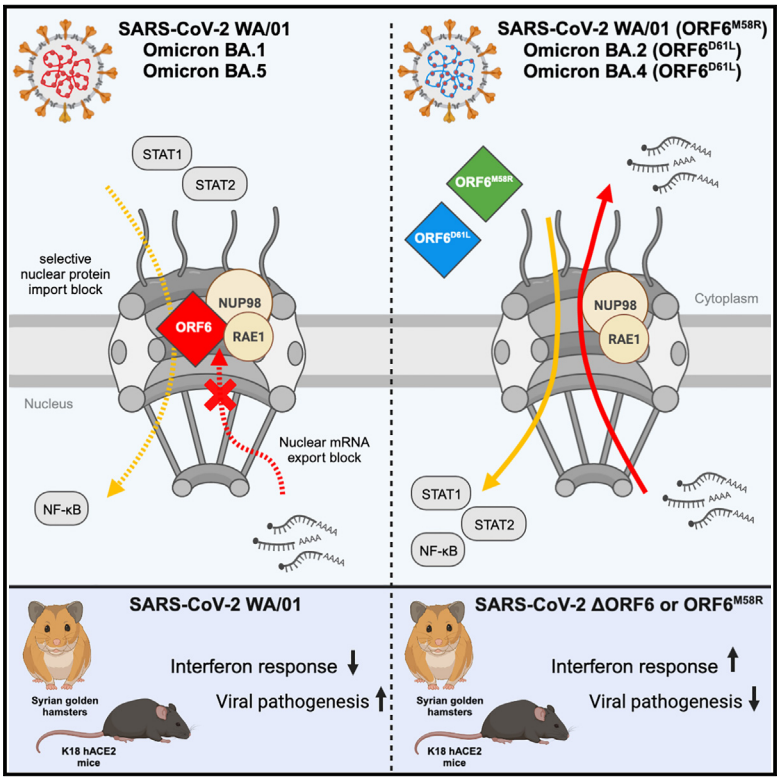

Highlights

- SARS-CoV-2 ORF6 antagonizes IFN-induced signaling during infection
- ORF6 binds Nup98-Rae1 and selectively inhibits nucleocytoplasmic trafficking
- ORF6 expression contributes to SARS-CoV-2 pathogenesis
- The D61L polymorphism disrupts ORF6 protein functions at the NPC

Authors

Thomas Kehrer, Anastasija Cupic, Chengjin Ye, ..., Luis Martinez-Sobrido, Adolfo García-Sastre, Lisa Miorin

Correspondence

adolfo.garcia-sastre@mssm.edu (A.G.-S.), lisa.miorin@mssm.edu (L.M.)

In brief

Kehrer, Cupic et al. dissect the role of ORF6 in the host response to SARS-CoV-2 infection. ORF6 is an innate immune antagonist that binds to Nup98-Rae1 and suppresses host gene expression by selectively inhibiting nucleocytoplasmic trafficking. ORF6 loss-of-function mutations result in SARS-CoV-2 attenuation both *in vitro* and *in vivo*.

Kehrer et al., 2023, Cell Host & Microbe *31*, 1–17
October 11, 2023
https://doi.org/10.1016/j.chom.2023.08.003

CellPress

Please cite this article in press as: Kehrer et al., Impact of SARS-CoV-2 ORF6 and its variant polymorphisms on host responses and viral pathogenesis, Cell Host & Microbe (2023), https://doi.org/10.1016/j.chom.2023.08.003

Cell Host & Microbe

CellPress
OPEN ACCESS

Article

Impact of SARS-CoV-2 ORF6 and its variant polymorphisms on host responses and viral pathogenesis

Thomas Kehrer,[1,2,23] Anastasija Cupic,[1,2,23] Chengjin Ye,[3] Soner Yildiz,[1,4] Mehdi Bouhaddou,[5,6,7,8,9,10,11] Nicholas A. Crossland,[12,13] Erika A. Barrall,[1,2] Phillip Cohen,[1,2] Anna Tseng,[12,13] Tolga Çağatay,[14] Raveen Rathnasinghe,[1,2,4] Daniel Flores,[1,4] Sonia Jangra,[1,4] Fahmida Alam,[1,4] Ignacio Mena,[1,4] Sadaf Aslam,[1,4] Anjali Saqi,[15] Magdalena Rutkowska,[1,2] Manisha R. Ummadi,[5,6,7,8] Giuseppe Pisanelli,[1,4,16] R. Blake Richardson,[1] Ethan C. Veit,[1,2] Jacqueline M. Fabius,[5,6,7] Margaret Soucheray,[5,6,7,8] Benjamin J. Polacco,[5,6,7,8] Baran Ak,[1] Arturo Marin,[1,4] Matthew J. Evans,[1] Danielle L. Swaney,[5,6,7,8] Ana S. Gonzalez-Reiche,[17] Emilia M. Sordillo,[18] Harm van Bakel,[1,17,19] Viviana Simon,[1,4,18,20,21] Lorena Zuliani-Alvarez,[5,6,7,8] Beatriz M.A. Fontoura,[14] Brad R. Rosenberg,[1] Nevan J. Krogan,[5,6,7,8] Luis Martinez-Sobrido,[3] Adolfo García-Sastre,[1,4,18,20,22,24,*] and Lisa Miorin[1,4,*]

[1]Department of Microbiology, Icahn School of Medicine at Mount Sinai, New York, NY 10029, USA
[2]Graduate School of Biomedical Sciences, Icahn School of Medicine at Mount Sinai, New York, NY 10029, USA
[3]Texas Biomedical Research Institute, San Antonio, TX 78227, USA
[4]Global Health Emerging Pathogens Institute, Icahn School of Medicine at Mount Sinai, New York, NY 10029, USA
[5]QBI COVID-19 Research Group (QCRG), San Francisco, CA 94158, USA
[6]Quantitative Biosciences Institute (QBI), University of California, San Francisco, San Francisco, CA 94158, USA
[7]J. David Gladstone Institutes, San Francisco, CA 94158, USA
[8]Department of Cellular and Molecular Pharmacology, University of California, San Francisco, San Francisco, CA 94158, USA
[9]Department of Microbiology, Immunology, and Molecular Genetics (MIMG), University of California, Los Angeles, Los Angeles, CA 90024, USA
[10]Institute for Quantitative and Computational Biosciences (OCBio), University of California, Los Angeles, Los Angeles, CA 90024, USA
[11]Molecular Biology Institute, University of California, Los Angeles, Los Angeles, CA 90024, USA
[12]National Emerging Infectious Diseases Laboratories, Boston University, Boston, MA 02215, USA
[13]Department of Pathology and Laboratory Medicine, Boston University Chobanian & Avedisian School of Medicine, Boston, MA 02118, USA
[14]Department of Cell Biology, University of Texas Southwestern Medical Center, Dallas, TX 75390, USA
[15]Department of Pathology and Cell Biology, Columbia University Medical Center, New York, NY 10032, USA
[16]Department of Veterinary Medicine and Animal Production, University of Naples Federico II, 80137 Naples, Italy
[17]Department of Genetics and Genomic Sciences, Icahn School of Medicine at Mount Sinai, New York, NY 10029, USA
[18]Department of Pathology, Molecular, and Cell-Based Medicine, Icahn School of Medicine at Mount Sinai, New York, NY 10029, USA
[19]Icahn Genomics Institute, Icahn School of Medicine at Mount Sinai, New York, NY 10029, USA
[20]Department of Medicine, Division of Infectious Diseases, Icahn School of Medicine at Mount Sinai, New York, NY, USA
[21]Center for Vaccine Research and Pandemic Preparedness (C-VARPP), Icahn School of Medicine at Mount Sinai, New York, NY 10029, USA
[22]Tisch Cancer Institute, Icahn School of Medicine at Mount Sinai, New York, NY 10029, USA
[23]These authors contributed equally
[24]Lead contact
*Correspondence: adolfo.garcia-sastre@mssm.edu (A.G.-S.), lisa.miorin@mssm.edu (L.M.)
https://doi.org/10.1016/j.chom.2023.08.003

SUMMARY

Severe acute respiratory syndrome coronavirus 2 (SARS-CoV-2) encodes several proteins that inhibit host interferon responses. Among these, ORF6 antagonizes interferon signaling by disrupting nucleocytoplasmic trafficking through interactions with the nuclear pore complex components Nup98-Rae1. However, the roles and contributions of ORF6 during physiological infection remain unexplored. We assessed the role of ORF6 during infection using recombinant viruses carrying a deletion or loss-of-function (LoF) mutation in ORF6. ORF6 plays key roles in interferon antagonism and viral pathogenesis by interfering with nuclear import and specifically the translocation of IRF and STAT transcription factors. Additionally, ORF6 inhibits cellular mRNA export, resulting in the remodeling of the host cell proteome, and regulates viral protein expression. Interestingly, the ORF6:D61L mutation that emerged in the Omicron BA.2 and BA.4 variants exhibits reduced interactions with Nup98-Rae1 and consequently impairs immune evasion. Our findings highlight the role of ORF6 in antagonizing innate immunity and emphasize the importance of studying the immune evasion strategies of SARS-CoV-2.

Please cite this article in press as: Kehrer et al., Impact of SARS-CoV-2 ORF6 and its variant polymorphisms on host responses and viral pathogenesis, Cell Host & Microbe (2023), https://doi.org/10.1016/j.chom.2023.08.003

INTRODUCTION

Despite the rapid development of vaccines and antiviral treatments, the coronavirus disease 2019 (COVID-19) pandemic, caused by severe acute respiratory syndrome coronavirus 2 (SARS-CoV-2), still remains a major global health concern (https://covid19.who.int). The clinical presentations of COVID-19 involve a broad range of symptoms, from asymptomatic infections to severe disease, normally characterized by excessive induction of proinflammatory cytokines, with an overall fatality rate near 1%.[1,2] While the determinants for disease outcome are not completely understood, numerous studies have suggested that the inability to mount a timely and effective antiviral interferon (IFN) response promotes viral persistence and tissue damage, contributing to SARS-CoV-2 virulence and COVID-19 severity.[1,3,4] In this regard, inborn errors of immunity affecting the Toll-like receptor 3 (TLR3) or IFN pathway, and the presence of neutralizing autoantibodies against type I IFN,[5,6] have been identified in a subset of severe COVID-19 patients. Furthermore, several viral proteins have been described to inhibit or suppress innate immune activation at different levels,[7–9] highlighting the importance of type I IFN in the defense against SARS-CoV-2 infection. Among these proteins, the non-structural protein NSP1 has been shown to inhibit antiviral gene expression by inhibiting host translation,[10] blocking nuclear export of cellular transcripts,[11,12] and inducing host mRNA cleavage.[13,14] The accessory protein ORF9B antagonizes IFN induction by interacting with TOM70 and inhibiting mitochondrial recruitment of TBK1 and IRF3.[15,16] In addition, SARS-CoV-2 ORF6 was found to directly interact with the Nup98-Rae1 complex to disrupt karyopherin-mediated nuclear import of STAT1 and STAT2,[8,17,18] and to contribute to the inhibition of mRNA export that we and others have observed during infection.[19–21]

As the virus evolved since its initial introduction into humans, new SARS-CoV-2 variants have emerged with major genomic changes that confer resistance to neutralizing antibodies and exhibit increased transmissibly and virulence.[22,23] Remarkably, we have previously shown that such variants of concern (VOCs), in addition to gaining spike (S) mutations that mediate antibody escape and alter virus entry into human cells, also evolved non-S mutations that result in increased expression of key viral innate immune antagonists such as ORF9B and ORF6, and enhanced innate immune suppression.[24] In this study, we closely dissect the impact of ORF6 and its recently emerged variant polymorphisms on the host response to SARS-CoV-2 infection to gain more detailed insights into the mechanisms employed by SARS-CoV-2 to escape innate antiviral responses and drive COVID-19 pathogenesis.

RESULTS

ORF6 expression is essential for the inhibition of STAT nuclear import during infection

We and others have previously shown that the SARS-CoV-2 accessory protein ORF6 directly interacts with Nup98-Rae1 at the nuclear pore complex (NPC) to disrupt STAT nuclear translocation and antagonize IFN signaling.[8,9,17,18] In this study, we employed our previously described recombinant SARS-CoV-2 virus system[25–27] to further assess the role of ORF6 in the modulation of the innate immune response in the context of infection. As shown in Figure 1A, in addition to a recombinant SARS-CoV-2 wild-type (WT) virus (rSARS-CoV-2 WT), we generated a virus carrying a deletion of the ORF6 coding sequence (rSARS-CoV-2 ΔORF6), as well as a virus with the ORF6^{M58R} mutation (rSARS-CoV-2 ORF6^{M58R}) previously shown to abolish binding to the Nup98-Rae1 complex.[8] The presence of the ORF6 deletion and ORF6^{M58R} mutation were validated by genome sequencing of the viral stocks (Figure S1).

Next, we monitored the replication kinetics of the different recombinant viruses in both Vero E6 and A549-ACE2 cells. Interestingly, while infection of Vero E6 cells did not reveal significant differences in viral titers at any of the time points analyzed, we found that both the ORF6-mutant viruses replicated to lower titers than the WT virus in A549-ACE2 cells (Figures 1B and 1C). In addition, the ORF6-deficient virus was also attenuated in human-derived tracheal/bronchial epithelial (HTBE) cells cultured at the air-liquid interface (ALI), yet the differences were less pronounced than in the A549-ACE2 cells (Figure 1D). As we previously showed that ORF6 antagonizes IFN signaling downstream of STAT phosphorylation,[8] we then assessed the ability of the ORF6 mutant viruses to inhibit STAT phosphorylation and nuclear translocation. As expected, upon treatment of Vero E6 with recombinant IFN, we observed no differences in the levels of total or phosphorylated STAT1 and STAT2 across conditions (Figure 1E). However, STAT2 nuclear translocation was effectively rescued in cells infected with both the ORF6-deficient and the ORF6^{M58R} viruses (Figure 1F). Importantly, these results were also confirmed in A549-ACE2 cells that can endogenously trigger IFN induction and subsequent STAT phosphorylation and nuclear translocation in response to infection (Figures 1G and 1H). Of note, A549-ACE2 cells showed similar levels of STAT1/2 phosphorylation upon infection with the WT or ORF6-mutant viruses, suggesting that while ORF6 expression plays a major role in the antagonism of IFN signaling, its role in the inhibition of IFN induction during infection might be redundant.

Finally, to confirm the interaction of ORF6 with the Nup98-Rae1 complex in the context of infection, we immunoprecipitated endogenous Nup98 in A549-ACE2 cells that were either mock infected or infected with the three different recombinant viruses. In agreement with our earlier findings, both ORF6 and Rae1 co-immunoprecipitated with Nup98 in cells infected with rSARS-CoV-2 WT, while only Rae1 was efficiently pulled down by Nup98 in cells infected with the mutant viruses, as expected (Figure 1I). All together, these results indicate that ORF6 binds to the Nup98-Rae1 complex during infection and that such virus-host interaction plays a major role in the antagonism of the IFN signaling pathway by disrupting STAT nuclear translocation.

ORF6 selectively blocks nuclear import of transcription factors

Next, to further investigate the role of ORF6 in the subversion of other important pathways involved in the host antiviral response, we closely looked at its ability to inhibit IRF3 and NF-κB nuclear translocation. In agreement with previous findings,[8,9,28] we show that ectopic expression of ORF6, but not of ORF6^{M58R}, was able to block RIG-I-2CARD-mediated IRF3-GFP nuclear translocation (Figure 2A) as well as IRF3-dependent gene expression (Figure 2B). However, p65 nuclear translocation and NF-κB reporter

Please cite this article in press as: Kehrer et al., Impact of SARS-CoV-2 ORF6 and its variant polymorphisms on host responses and viral pathogenesis, Cell Host & Microbe (2023), https://doi.org/10.1016/j.chom.2023.08.003

CellPress
OPEN ACCESS

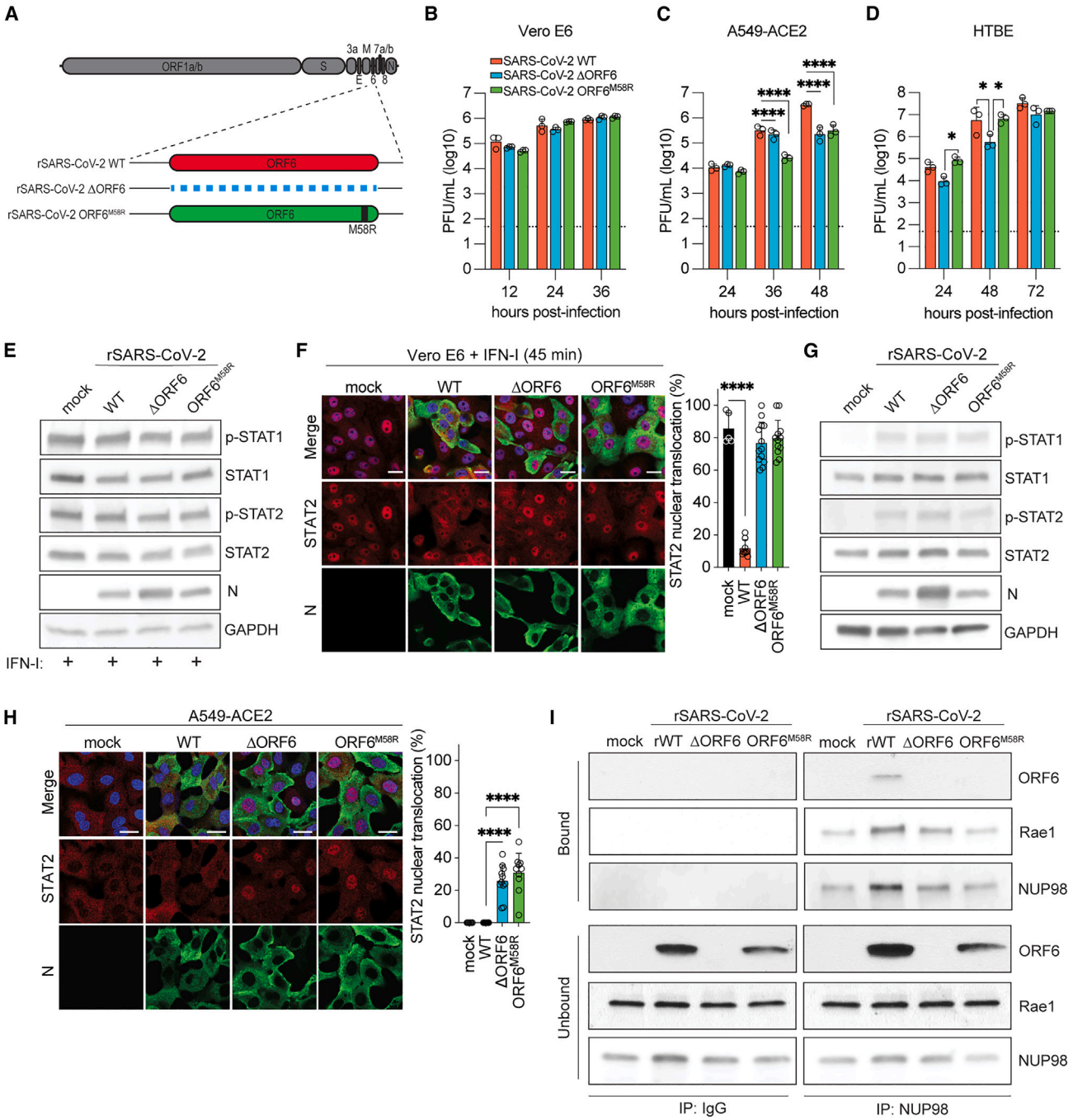

Figure 1. ORF6 is essential for inhibition of STAT1/2 nuclear import and optimal replication in IFN-competent cells

(A) Schematic illustration of the genome organization of recombinant viruses used in our studies.

(B and C) (B) Growth curve in Vero E6 cells or (C) A549-ACE2 cells infected at MOI 0.1. Data is presented as mean ± SD (n = 3).

(D) Growth curve in HTBE cultures infected with 10^5 plaque-forming unit (PFU). Data is presented as mean ± SD (n = 3).

(E) Vero E6 cells were infected with the indicated viruses at MOI 0.5 for 24 h before treatment with universal IFN and western blot analysis.

(F) Vero E6 cells were infected with the indicated viruses and then treated with IFN universal prior to fixation. The subcellular localization of STAT2 was analyzed by confocal microscopy. STAT2 nuclear translocation in infected cells was quantified from ≥150 cells per condition (n = 2). The scale is represented by the white bar (20 μm).

(G) A549-ACE2 cells were infected with the indicated viruses for 24 h. Expression and phosphorylation status of the indicated proteins was determined by western blot.

(legend continued on next page)

Please cite this article in press as: Kehrer et al., Impact of SARS-CoV-2 ORF6 and its variant polymorphisms on host responses and viral pathogenesis, Cell Host & Microbe (2023), https://doi.org/10.1016/j.chom.2023.08.003

activation upon TNF-α treatment were not affected (Figures 2C and 2D). For these experiments, expression of hepatitis C virus NS3/4A and TRIM9 were used as positive control for inhibition of gene expression upstream of the IRF3- and NF-κB-responsive promoters, respectively.[29,30] To address the relevance of these findings in the context of infection, we then infected A549-ACE2 cells and quantified both IRF3 and NF-κB nuclear translocation by immunofluorescence analysis. As expected, we found that p65 efficiently translocated into the nucleus of cells infected with both recombinant viruses (Figure 2E). However, we did not find significant differences in IRF3 nuclear translocation at any of the time points analyzed (Figure 2F). Importantly, these data were also consistent with the similar levels of IRF3 and NF-κB phosphorylation detected by western blot (Figure 2G). This suggests that while ORF6 has the potential to block IRF3 nuclear translocation by interfering with karyopherin-mediated nuclear import, its function in the inhibition of IFN induction during infection is likely redundant. Presumably, this is due to the expression of other viral antagonists that are acting more upstream in the pathway and contribute to the poor and delayed IRF3 activation by SARS-CoV-2 that we and others have observed in A549-ACE2 cells.[14]

ORF6 disrupts mRNA nuclear export and inhibits host gene expression

As we and others have previously shown that SARS-CoV-2 infection results in the inhibition of host mRNA nuclear export,[11,12] we sought to investigate whether the ORF6:Nup98-Rae1 interaction could contribute to this process. To this end, we first transfected HEK293T cells with SARS-CoV-2 ORF6, ORF6^{M58R} or empty vector, and looked at the intracellular distribution of bulk poly(A) RNA levels by fluorescence *in situ* hybridization (RNA-FISH). Remarkably, while bulk poly(A) RNA was localized throughout the cell in empty vector transfected cells, expression of WT ORF6, but not ORF6^{M58R}, resulted in a significant increase in the nuclear to cytoplasmic ratio (N/C) of poly(A) RNA (Figure 3A), indicating that ORF6 may also disrupt Nup98/Rae1 mRNA nuclear export functions. Next, to further address the contribution of ORF6 to the inhibition of mRNA export during infection, we performed nucleocytoplasmic fractionation to assess the subcellular distribution of a set of transcripts previously reported to be retained into the nucleus of SARS-CoV-2-infected cells.[12] Importantly, since differences in poly(A) RNA levels could be influenced by additional processes, such as hyperadenylation of host mRNAs in the nucleus and accumulation of viral mRNAs in the cytoplasm, this approach would allow for a more direct assessment of host mRNA export. In agreement with our RNA-FISH data in overexpression, we found a significant reduction of nuclear mRNA retention in cells infected with both ORF6 mutant viruses as compared with WT (Figure 3B). These data were also corroborated by assessing the nucleocytoplasmic distribution of NFKB1 and NUAK2 mRNAs upon virus infection by single-molecule RNA-FISH (smRNA-FISH). Indeed, a higher percentage of nuclear mRNA for both NFKB1 and NUAK2 was observed in cells infected with rSARS-CoV-2 WT as compared with rSARS-CoV-2 ΔORF6 or ORF6^{M58R} (Figures 3C and 3D). Notably, the absolute number of nuclear smRNA transcripts for both NFKB1 and NUAK2 was significantly higher in cells infected with the WT virus (Figure S2A), suggesting that ORF6 expression triggers a block in mRNA nuclear export rather than a differential decay of mRNAs in the cytoplasm, and is likely to inhibit host gene expression during infection.

To further explore the global effect of ORF6 on host gene expression, we next performed mass spectrometry abundance proteomics and phosphoproteomics (Figures 3E–3G and S2B–S2D). Importantly, in these experiments A549-ACE2 cells were infected at an MOI of 2 to ensure comparable infections rates (Figure S2B, left). As expected, principal-component analysis (PCA) of the abundance proteomics data showed that infected cells clustered away from uninfected cells along the first principal component, suggesting a shift in protein expression upon infection (Figure S2C). In addition, cells infected with the ORF6-deficient virus clustered together with the ORF6^{M58R} infected samples, suggesting that ORF6 expression dramatically remodels host gene expression primarily by altering Nup98-Rae1 nuclear transport functions. In line with the observed ORF6-mediated disruption of nucleocytoplasmic trafficking, we found that cells infected with the mutant viruses showed an overall increase in host protein expression with respect to cells infected with rSARS-CoV-2 WT, while a comparison between the ORF6-mutant viruses indicated a more similar protein expression profile (Figures 3E and 3F). Interestingly, gene ontology (GO) analysis revealed that the top biological processes upregulated during infection with the mutant viruses are linked to mRNA metabolism and include RNA splicing, ribonucleoprotein biogenesis, RNA polymerase II elongation, among others (Figure 3G). Similar GO biological processes also appear to be regulated by ORF6 at the level of protein phosphorylation (Figure S2D).

ORF6 expression contributes to viral pathogenicity in Syrian golden hamsters

Next, to evaluate the role of ORF6 in the pathogenesis of SARS-CoV-2, we intranasally inoculated Syrian golden hamsters with either the parental or the ORF6-deficient virus (Figure 4A). Remarkably, we found that animals infected with the ORF6-deficient virus exhibited significantly reduced body weight loss and began to recover approximately 3 days earlier than animals infected with the WT virus (Figure 4B). However, we did not find significant differences in viral titers in both lung and nasal turbinates (Figure 4C). These results suggest that rather than the viral load, changes in the host response to the infection between the two viruses are likely to be responsible for the observed differences in morbidity. Next, to evaluate the impact of viral infection in the lungs of infected animals, we performed a detailed

(H) A549-ACE2 cells were infected with the indicated viruses for 24 h to assess the subcellular localization of STAT2 by immunofluorescence. STAT2 nuclear translocation in in infected cells was quantified from ≥150 cells per condition (n = 2). The scale is represented by the white bar (20 μm).
(I) A549-ACE2 cells were infected for 24 h and then subjected to immunoprecipitation of endogenous Nup98 followed by western blot analysis.
Data in (B)–(D) were analyzed by two-way ANOVA Tukey's multiple comparison test: ****$p < 0.0001$; *$p \leq 0.05$. Data in (F) and (H) were analyzed by ordinary one-way ANOVA using Tukey's multiple comparison test: ****$p < 0.0001$. Graphs were generated with PRISM (version 9).

Please cite this article in press as: Kehrer et al., Impact of SARS-CoV-2 ORF6 and its variant polymorphisms on host responses and viral pathogenesis, Cell Host & Microbe (2023), https://doi.org/10.1016/j.chom.2023.08.003

CellPress
OPEN ACCESS

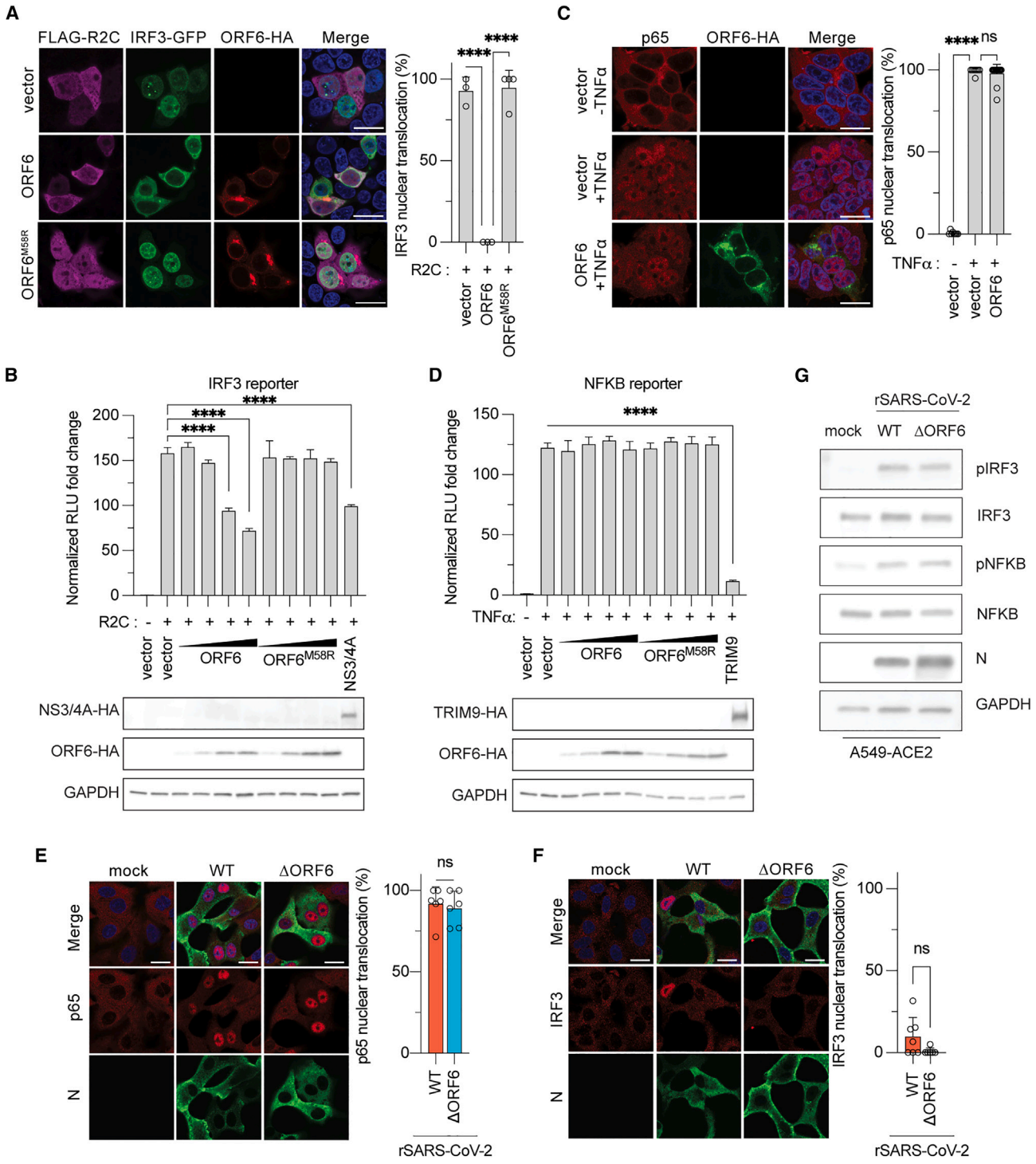

Figure 2. ORF6 selectively blocks nuclear import of innate immune transcription factors

(A) HEK293T cells were transfected with ORF6, ORF6-M58R or empty vector along with FLAG-RIG-I-2CARD and IRF3-GFP. Nuclear translocation of IRF3-GFP in control and ORF6/RIG-I-2CARD double-positive cells was quantified from three fields of view collected from two independent experiments. The scale is represented by the white bar (20 μm).

(B) HEK293T cells were transfected with plasmids expressing ORF6 or ORF6-M58R or HCV NS3/4A, along with FLAG-RIG-I-2CARD and a plasmid encoding an IRF3-firefly luciferase reporter. Data are represented as mean ± SD (n = 3). Cell lysates from the reporter assay were analyzed by western blot.

(C) HEK293T cells were treated with TNF-α 24 h post-transfection with the indicated plasmids and the subcellular localization of p65 was assessed immunofluorescence. Nuclear translocation of p65 was quantified from four fields of view collected from two independent experiments. The scale is represented by the white bar (20 μm).

(legend continued on next page)

Please cite this article in press as: Kehrer et al., Impact of SARS-CoV-2 ORF6 and its variant polymorphisms on host responses and viral pathogenesis, Cell Host & Microbe (2023), https://doi.org/10.1016/j.chom.2023.08.003

histopathological evaluation on lungs collected at 2, 4, and 6 days post-infection (dpi). Temporal histologic phenotypes observed in the two infected cohorts were not readably discernible qualitatively and were consistent with previous reports of COVID-19 in Syrian golden hamsters.[31] In brief, this was characterized by necrosuppurative bronchiolitis at 2 dpi that progressed to bronchointerstitial pneumonia with edema and hemorrhage at 4 dpi, culminating in a reparative response reflected by bronchiolar and alveolar type 2 (AT2) cell hyperplasia and bronchiolization of alveoli at 6 dpi. However, subsequent quantitative tissue classification of H&E-stained lung sections revealed that WT-virus-infected animals exhibited a significant increase in the percentage of consolidated lung area at 6 dpi compared with animals infected with the ORF6 deficient virus (Figure 4E). Histologically this was reflected by an increased proliferative index as determined by the percentage of nuclei expressing Ki67, which predominated in areas of AT2 cell hyperplasia (Figure 4F). Taken together these findings suggest that a more robust reparative response occurs in WT-infected hamsters attributable to increase lung injury at earlier time points that correlates with the difference in lung/bodyweight ratio at 6 dpi (Figure 4D).

Given the prominent role of ORF6 in the inhibition of IFN signaling, we next sought to assess STAT1 nuclear translocation in the lungs of the infected animals by immunohistochemistry (IHC). In agreement with our previous findings *in vitro*, we found that pSTAT1 was mainly localized in the cytoplasm of S-positive cells within the bronchioles of rSARS-CoV-2 WT-infected animals. However, approximately 80% of the double-positive cells in the lungs of animals infected with the ORF6-deficient virus showed a nuclear pSTAT1 staining at both 2 and 4 dpi (Figure 4G). This is also consistent with the ability of ORF6 to inhibit STAT nuclear translocation in a Syrian golden hamster cells line (BHK-21) (Figure S3). Importantly, the impact of ORF6 in the inhibition of IFN signaling was also corroborated by the augmented Mx1 protein expression detected by IHC at 6 dpi in the lungs of the rSARS-CoV-2 ΔORF6 infected animals (Figure 4H).

Lastly, since infection with SARS-CoV-2 is not lethal in the Syrian golden hamster model, we evaluated the ability of the ORF6-deficient virus to trigger a protective immune response against a SARS-CoV-2 WT challenge (Figure S4). As expected, infection of mock-treated hamsters led to approximately 20% body weight loss by 6 dpi. However, no changes in body weight were observed in hamsters previously infected with the WT or ΔORF6 virus (Figure S4B). Consistently, similar levels of serum immunoglobulin G (IgG) against full-length viral S protein (Figure S4D), and almost undetectable levels of infectious virus in the nasal washes (Figure S4C), were found in hamsters previously challenged with the recombinant WT and ORF6-deficient viruses.

ORF6 modulates viral protein expression

Based on the observation that N protein expression was consistently upregulated in cells infected with the ORF6-deficient as compared with the WT and the ORF6^{M58R} virus throughout our experiments (Figures 1E, 1G, 2G, and S2B, right), we hypothesized that ORF6 could play a role in the modulation of viral gene expression. To test this hypothesis, we first quantified the differences in viral protein levels between rSARS-CoV-2 WT and ΔORF6 infected cells from our global abundance proteomics. As shown in Figure 5A, our analysis revealed significant differences in the relative abundance of several ORF1a/b- and subgenomic RNA (sgRNA)-derived viral proteins, despite very similar infection rates (Figure S2B, left). Remarkably, we found that the levels of all ORF1ab-derived NSPs, with the exception of NSP15 and NSP16, were significantly downregulated in rSARS-CoV-2 ΔORF6-infected cells. However, expression of several structural and accessory proteins, namely S, ORF3A, M, ORF7A, N and ORF9B, was upregulated compared with WT-virus-infected cells (Figure 5A). Notably, the phenotype of reduced NSP levels and increased expression of sgRNA-derived viral proteins by the ORF6-deficient virus compared with WT and the ORF6^{M58R} virus was also validated by western blot analysis (Figure 5B).

Next, to investigate whether ORF6 modulates viral protein expression at a transcriptional or post-transcriptional (translation and/or protein stability) step, we infected cells with either rSARS-CoV-2 WT or ΔORF6 and quantified the levels of sgRNA/total viral reads and sgRNA/gRNA by bulk mRNA sequencing and quantitative real-time PCR, respectively (Figures 5C and 5D). As shown in Figure S2E, similar infection rates were achieved by the two viruses under these experimental conditions. Interestingly, we found that despite the remarkable modulation of viral protein expression, the production of both genomic and subgenomic transcripts was only marginally affected in cells infected with the ORF6-deficient virus (Figures 5C and 5D).

To rule out the possibility that the observed phenotype was due to the 197-nucleotides deletion in the ORF6 genomic sequence rather than the lack of protein expression, we then generated a rSARS-CoV-2 virus carrying a premature STOP codon in ORF6 (rSARS-CoV-2 ORF6^{STOP}) and measured viral protein expression at 24 h post-infection by western blot and flow cytometry (Figures 5E and S5). In agreement with our previous findings, while expression of both NSPs and accessory proteins was comparable in cells infected with rSARS-CoV-2 WT and ORF6^{M58R}, both ORF6-deficient viruses showed reduced NSP1 levels along with an increase in S and N expression. Thus, these results suggest that ORF6 plays a previously unrecognized role in the virus life cycle and is critical for the post-transcriptional modulation of viral protein expression. Importantly,

(D) HEK293T cells were transfected with an NF-κB-firefly luciferase reporter along with the indicated plasmids. At 24 h post-transfection, cells were treated with TNF-α and used for dual luciferase reporter assay. Data are represented as mean ± SD(n = 3). Cell lysates were analyzed by western blot.
(E) A549-ACE2 cells were infected and processed for assessment of the subcellular localization of p65 by immunofluorescence. p65 nuclear translocation in infected cells was quantified from ≥150 cells per condition (n = 2). The scale is represented by the white bar (20 μm).
(F) Same as (E) but subcellular localization of IRF3 was assessed.
(G) A549-ACE2 cells were infected with the indicated viruses for 24 h. Expression and phosphorylation status of the indicated proteins was determined by western blot.
Data in (A)–(D) were analyzed by ordinary one-way ANOVA using Tukey's multiple comparison test: ****$p < 0.0001$; ns, not statistically significant. Data in (E) and (F) were analyzed by two-tailed unpaired Student's t test: ns, not statistically significant. Graphs were generated with GraphPad PRISM (version 9).

Please cite this article in press as: Kehrer et al., Impact of SARS-CoV-2 ORF6 and its variant polymorphisms on host responses and viral pathogenesis, Cell Host & Microbe (2023), https://doi.org/10.1016/j.chom.2023.08.003

CellPress
OPEN ACCESS

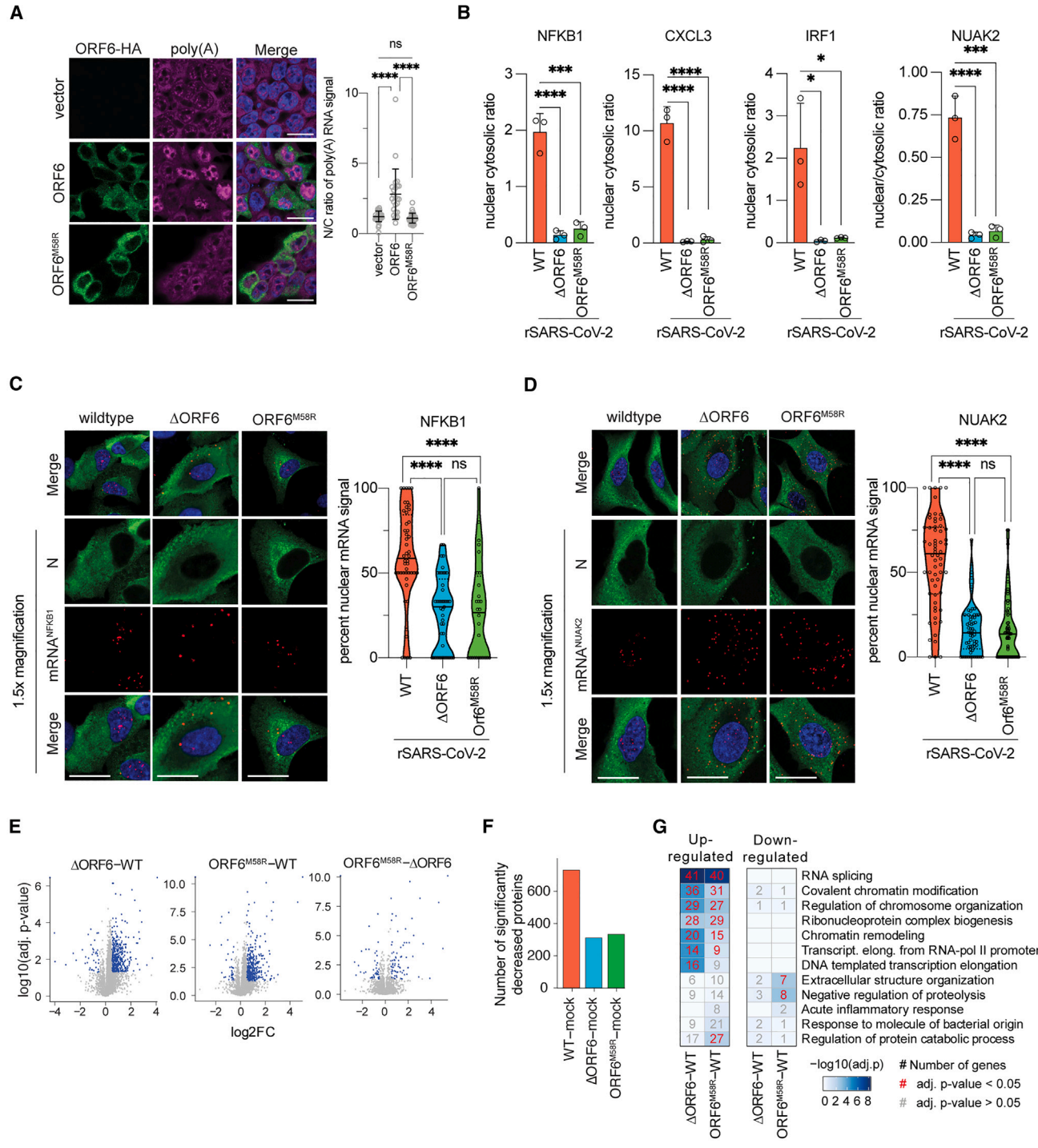

Figure 3. ORF6 disrupts mRNA nuclear export and contributes to host translational shutdown during infection

(A) HEK293T were transfected with the indicated plasmids and subjected to poly(A) RNA immune-FISH analysis. The N/C ratio of poly(A) RNA signals in individual cells is shown for the various depicted conditions. The graph shows mean ± SD (n = 3). Scale bar, 20 μm.

(B) A549-ACE2 cells were infected with the indicated viruses for 24 h and then subject to subcellular fractionation. Total RNA was isolated and subjected to real-time-qPCR. Graph shows N/C ratio of indicated transcripts after normalization to respective compartment markers. The graph shows mean ± SD (n = 3).

(C) A549-ACE2 cells were infected 24 h before fixation and processed for smRNA-FISH to determine subcellular localization of NFKB1 transcripts. Transcript localization in infected cells was quantified from ≥30 cells per condition from three biological replicates. Data are shown as violin plots, solid line marks median, and dashed lines mark quartiles. Scale bar, 20 μm.

(D) Same as (C) but localization of NUAK2 transcripts was quantified.

(legend continued on next page)

while the molecular mechanisms underlying this ORF6 function are still under investigation, the similar levels of N protein expression observed in rSARS-CoV-2 WT and ORF6^{M58R}-infected cells (Figures 1E, 1G, and S2B), strongly suggest that this process is independent of the interaction of ORF6 with the Nup98-Rae1 complex.

Disruption of Nup98/Rae1 nuclear transport functions contributes to SARS-CoV-2 pathogenesis in K18 human ACE2 transgenic mice

Given the impact of ORF6 on the modulation of viral protein expression, we next sought to specifically assess the contribution of the ORF6:Nup98-Rae1 interaction to viral pathogenicity in K18 hACE2 mice. To this end, we inoculated animals with either the parental rSARS-CoV-2 WT or the ORF6^{M58R} mutant virus that exhibits impaired ORF6-mediated NPC functions while maintaining unaltered expression of viral proteins. In addition, mice were also treated with IgG control or anti-IFNAR1 blocking antibody (rIFNAR Ab), to inhibit type I IFN signaling (Figure 6A). We observed a similar decrease in body weight percentages up to 6 dpi in control- or rIFNAR Ab-treated animal infected with the parental rSARS-CoV-2 virus (Figure 6B). However, while 20% of the IgG-treated mice survived infection, all rIFNAR Ab-treated mice succumbed to viral infection by 8 dpi (Figure 6C), possibly due to the increased viral load we found, particularly in the brain, upon inhibition of type I IFN signaling (Figure 6D). Similar to our findings in Syrian golden hamsters, IgG-treated mice infected with the ORF6^{M58R} mutant virus showed lung and nasal turbinate titers comparable to rSARS-CoV-2 WT-infected animals at 5 dpi. However, no virus was detected in the brains of 2 out of 4 mice infected with rSARS-CoV-2 ORF6^{M58R}, suggesting that ORF6 NPC functions may confer an increased propensity for neuroinvasiveness in this animal model. Notably, as indicated by the differences in weight loss and survival, despite the ability of ORF6 to block STAT1 nuclear translocation in murine cells (Figure S6), the ORF6^{M58R} mutant virus was attenuated in both control and rIFNAR Ab-treated mice (Figures 6B and 6C). Although further studies are warranted, these results may either reflect the protective effects of IFN-λ that can still signal in the presence of IFNAR1 blocking antibodies,[32] or suggest that by disrupting nucleocytoplasmic trafficking ORF6 alters the activity of additional factors (other than STAT1 and STAT2) involved in disease pathogenesis.

The ORF6^{D61L} mutation shared by Omicron variants BA.2 and BA.4 disrupts protein functions at the NPC

Despite the sporadic emergence of frameshifts and/or nonsense mutations in ORF6 during the current COVID-19 pandemic, such mutations have not spread dominantly in the viral population until recently.[28] We previously reported that the upregulation of key viral innate antagonists, including ORF6 and ORF9b, by the Alpha VOC likely contributed to its enhanced transmission and human adaptation.[24] Interestingly, a single point mutation in ORF6 (ORF6^{D61L}) recently emerged in the Omicron subvariants BA.2, BA.4, but was not present in the subsequently dominant BA.5 subvariant, which otherwise shares a lot of similarities with BA.4.[23] In addition, the ORF6^{D61L} polymorphism is currently circulating again with the new XBB subvariants. The ORF6 D61 residue is located in close proximity to the key M58 residue at the C-terminal tail (CTT) of the protein that directly binds to the RNA-binding pocket of the Nup98-Rae1 complex (Gao et al.,[17] Li et al.,[19] and accompanying paper). Therefore, we sought to investigate the impact of this mutation on the ability of ORF6 to interact with the Nup98-Rae1 complex and inhibit IFN signaling.

Strikingly, we found that binding of ORF6^{D61L} to Nup98-Rae1 was significantly reduced, indicating that the D61 residue is important for interaction with the NPC (Figure 7A). Next, we examined the impact of the D61 mutation on nucleo-cytoplasmic trafficking. We found that expression of ORF6^{D61L} was unable to block IFN- and 2CARD-RIGI-mediated nuclear translocation of STAT2 and IRF3, respectively (Figures 7B and 7C). In addition, STAT2- and IRF3-dependent gene expression was also not affected by ORF6^{D61L} overexpression (Figures S7A and S7B). As expected, NF-κB nuclear translocation and NF-κB reporter activation were also not impaired by ORF6^{D61L} (Figures S7C and S7D). Importantly, when we looked at the intracellular distribution of bulk poly(A) RNA levels by RNA-FISH, we found that ORF6^{D61L}, unlike WT ORF6, did not significantly increase the N/C ratio of poly(A) RNA in the cell. This indicates that the D61L mutation also interferes with the ability of ORF6 to disrupt Nup98-Rae1 mRNA nuclear export functions (Figure S7E).

Because of the significant impairment of ORF6 functions at the NPC by the D61L mutation, we then tested whether analogous observations could be made during infection with Omicron subvariants that harbor the different ORF6 polymorphisms. In agreement with our findings, we observed a significant increase in the levels of IFN-dependent STAT2 nuclear translocation in cells infected with Omicron subvariants carrying the ORF6^{D61L} mutation (BA.2 and BA.4) as compared with cells infected with the WA/01 ancestral strain or Omicron BA.1 and BA.5 (Figure 7D; Table S2). In addition, cells infected with the BA.2 and BA.4 subvariants also exhibited a significant reduction in the levels of nuclear NUAK2 mRNA as detected by smRNA-FISH (Figure 7E), indicating that this polymorphism is sufficient to alter the mRNA export block observed during infection. Furthermore, as shown in Figure 7F, we found that BA.5 replicates more efficiently than ORF6^{D61L} expressing BA.2 and BA2.9.2 in IFN-competent A549-ACE2 cells.

(E–G) A549-ACE2 cells were infected and processed for mass spectrometry analysis (see STAR Methods). The quantity of each protein was statistically compared between each condition generating a $\log_2$ fold change (log2FC) and adjusted p values. (E) Volcano plots of abundance proteomics depicting changes in protein expression for indicated comparisons (e.g., ΔORF6-WT indicates $\log_2$(ΔORF6/WT)), with $\log_2$ fold change (log2FC) on the x axis and adjusted p values on the y axis. (F) The number of proteins that significantly decrease (absolute value $\log_2$FC > 1 and adjusted $p < 0.05$) between each mutant and wild-type condition (blue dots from E), as indicated. (G) Gene ontology (GO) biological process gene set overrepresentation analysis using proteins either significantly upregulated or downregulated (blue dots from E) between each mutant and wild-type condition, as indicated. Numbers indicate the number of proteins mapping to each term, red numbers indicate a significant (adjusted p value < 0.05) enrichment, and gray numbers indicate a non-significant enrichment. Additionally, background colors in heatmap denote the $-\log_{10}$ adjusted p values (see colorbar).

Data in (A)–(D) were analyzed by ordinary one-way ANOVA using Tukey's multiple comparison test: ****$p < 0.0001$; ***$p < 0.001$; *$p \leq 0.05$; ns, not statistically significant. Data in (E)–(G) were analyzed as described in STAR Methods.

Please cite this article in press as: Kehrer et al., Impact of SARS-CoV-2 ORF6 and its variant polymorphisms on host responses and viral pathogenesis, Cell Host & Microbe (2023), https://doi.org/10.1016/j.chom.2023.08.003

CellPress
OPEN ACCESS

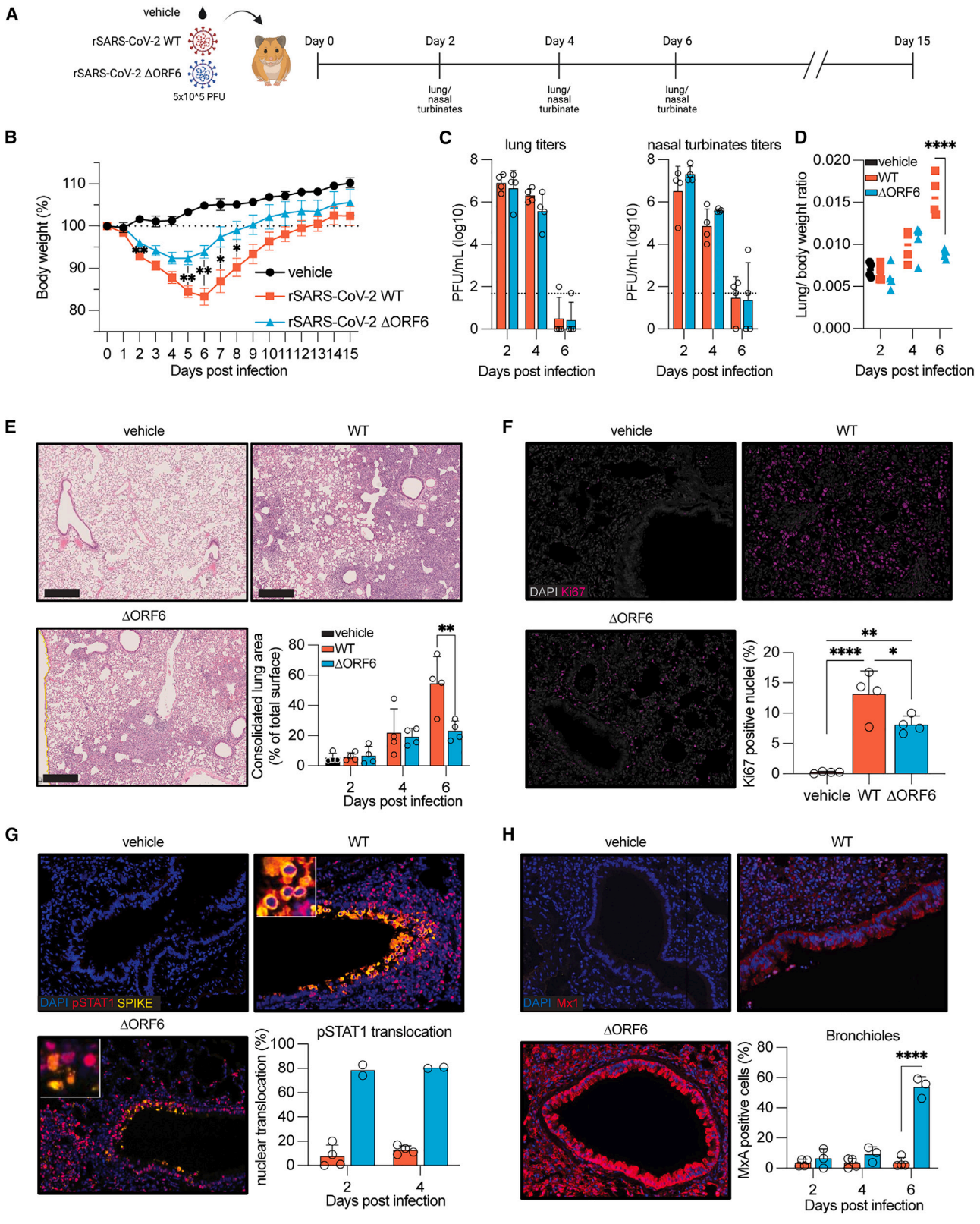

Figure 4. ORF6 plays a critical role in SARS-CoV-2 pathogenesis in Syrian hamsters

(A) Schematic of the *in vivo* experiment using Golden Syrian hamsters.

(B) Hamster weight as a percentage of their weight on day 0. Weight loss data are shown as mean ± SEM.

(legend continued on next page)

Please cite this article in press as: Kehrer et al., Impact of SARS-CoV-2 ORF6 and its variant polymorphisms on host responses and viral pathogenesis, Cell Host & Microbe (2023), https://doi.org/10.1016/j.chom.2023.08.003

All together, these results suggest that the D61L mutation significantly disrupts ORF6 protein functions at the NPC and impairs innate immune evasion with potential implications for viral fitness.

DISCUSSION

The innate immune response acts as a first line of defense against infection by upregulating IFN-stimulated genes (ISGs) expression and limiting virtually any step of the virus life cycle to promote viral clearance.[33] As a countermeasure, SARS-CoV-2 has evolved multiple strategies to suppress or at least interfere with the IFN response and enhance replication and transmission.[1,7,24,34] In this study, we used molecular and biochemical methods, combined with *in vivo* animal studies, to dissect the impact of the innate immune antagonist ORF6 on the host response to SARS-CoV-2 infection. Our results show that ORF6, by interacting with the Nup98-Rae1 complex at the nuclear pore, can interfere with nucleocytoplasmic trafficking in two distinct ways: by selectively inhibiting karyopherin-mediated nuclear import pathways and by modulating host cell mRNA export.

Using recombinant WT and ORF6-mutant viruses as well as recently emerged SARS-CoV-2 Omicron variants containing a D61L mutation in the CTT of the protein, we show that the ORF6-Nup98 interaction is required to block STAT1/2 nuclear translocation during infection, thereby inhibiting ISG expression, both *in vitro* and in the Syrian golden hamster model. In addition, we also found that ORF6 cannot prevent nuclear translocation of NF-κB p65, which has also been shown to be mediated by the classic karyopherin alpha/beta1 pathway,[35] pointing toward a selective inhibition of nuclear import. Interestingly, while it cannot be excluded that some cargos could traffic using an alternate route if the karyopherin alpha/beta1 pathway is blocked, such specificity may also suggest the existence of different subsets of Nup98-dependent and Nup98-independent cargo complexes. Further studies will be required to fully understand the molecular basis for this specificity.

A second common mechanism to inhibit host gene expression and downregulate innate antiviral defenses is to interfere with nuclear mRNA export,[36–38] and different viruses have been shown to target the Nup98-Rae1 complex to accomplish this effect.[39–42] We previously showed that SARS-CoV-2 infection inhibits host mRNA nuclear export and that the viral NSP1 protein contributes to this process by binding to the mRNA export receptor heterodimer NXF1-NXT1 and reducing its interaction with the NPC.[11] Since NXF1-NXT1 interacts with phenylalanine-glycine (FG) repeats on nucleoporins, such as Nup98, to mediate docking of messenger ribonucleoproteins (mRNPs) and facilitate trafficking trough the NPC,[43,44] we hypothesized that ORF6 could also interfere with this process. In addition, structural data have recently shown that, similarly to VSV M and herpesvirus ORF10 proteins,[41,42] the CTT of ORF6 directly interacts with the RNA-binding groove of the Nup98-Rae1 complex and competes for *in vitro* binding of single-stranded RNA.[17,19] Consistent with these notions, our results show that ORF6 indeed blocks Nup98-Rae1 mRNA export functions and contributes to the shutoff in protein synthesis that occurs during infection. Furthermore, we observed that the D61L mutation, shared by the Omicron variants BA.2, BA.4, and the currently circulating XBB.1.5 and XBB.1.16 sublineages, in addition to interfering with the ability of ORF6 to inhibit nuclear import, also influences its ability to block host mRNA export, which may have important implications for viral transmissibility and pathogenicity (see the related *Cell paper* by Bouhaddou et al.[45]). Since NSP1 has also been shown to inhibit host mRNA export, a better understanding of how ORF6 and NSP1 functions cooperate and/or complement each other during infection will be key to fully reveal the molecular mechanisms underlying innate immune antagonism by these viral proteins.

Consistent with a role of ORF6 in viral pathogenesis, Syrian Golden hamsters infected with rSARS-CoV-2 ΔORF6 experienced less body weight loss and reduced lung injury and AT2 cell hyperplasia, correlating with increased STAT2 translocation and ISG expression in lungs. In addition, the ORF6^{M58R} mutant virus that is unable to disrupt Nup98-Rae1 nuclear transport functions, also appeared to be less pathogenic in K18 human ACE2 mice. Surprisingly, this did not result in significant lower levels of viral replication in the respiratory tract of animals infected with rSARS-CoV-2 ΔORF6 or rSARS-CoV-2 ORF6^{M58R}. The impact of ORF6 function on viral replication might be too subtle to be able to detect in these experimental animal models. A small impact on viral replication *in vivo* associated with ORF6 function might also explain the circulation and transmission of Omicron variants containing a deleterious ORF6 polymorphism in humans. Nevertheless, these variants are less replicative in IFN-competent A549 cells than BA.5, lacking this polymorphism, but containing identical changes in S associated with immuno-evasion as compared with BA.4. In addition, *in vivo* competition experiments revealed that BA.5 outcompeted BA.2 in hamsters,[46] suggesting that BA.5 possesses superior viral fitness to BA.2, and that BA.5 human transmission dominance might have been at least in part mediated by the lack of the ORF6 D61L mutation (see the related *Cell paper* by Bouhaddou et al.[45]).

(C) Lung and nasal turbinates titers. Dashed line indicates the limit of detection for plaque assay (50 PFU/mL) (n = 4 per group). The graph shows mean ± SD.
(D) Lung to body weight ratio for animals sacrificed at the indicated days post-infection. Line indicates mean value (n = 4 per group).
(E) Representative images of lung H&E staining for all three groups of animals at day 6 post-infection. Graph shows the consolidated lung area at the indicated time points (n = 4 per group). Scale bar, 500 μm.
(F) Tissue sections from animals at day 6 post-infection were stained for DAPI and Ki67 (n = 4). Ki67-positive nuclei were quantified as described in methods. The graph shows mean ± SD.
(G) Tissue sections from indicated animals were stained for DAPI, pSTAT1, and SARS-CoV-2 spike. pSTAT1 nuclear translocation was quantified as described in STAR Methods. Images show representative staining from day 4 post-infection (n= 2-4 per group).
(H) Tissue sections from indicated animals were stained for DAPI and Mx1. Images show representative Mx1 staining from day 6 post-infection (n= 3-4 per group).
Data in (B) were analyzed using mixed-effects model analysis (REML) Šídák's multiple comparisons test: $^{**}p < 0.01$; $^{*}p \leq 0.05$. Data in (C)–(E) and (H) were analyzed by two-way ANOVA using Šídák's multiple comparisons test: $^{****}p < 0.0001$; $^{**}p < 0.01$. Data in (F) and (G) were analyzed by ordinary one-way ANOVA using Tukey's multiple comparison test: $^{****}p < 0.0001$; $^{**}p < 0.01$; $^{*}p \leq 0.05$. Graphs were generated with PRISM (version 9).

Please cite this article in press as: Kehrer et al., Impact of SARS-CoV-2 ORF6 and its variant polymorphisms on host responses and viral pathogenesis, Cell Host & Microbe (2023), https://doi.org/10.1016/j.chom.2023.08.003

CellPress
OPEN ACCESS

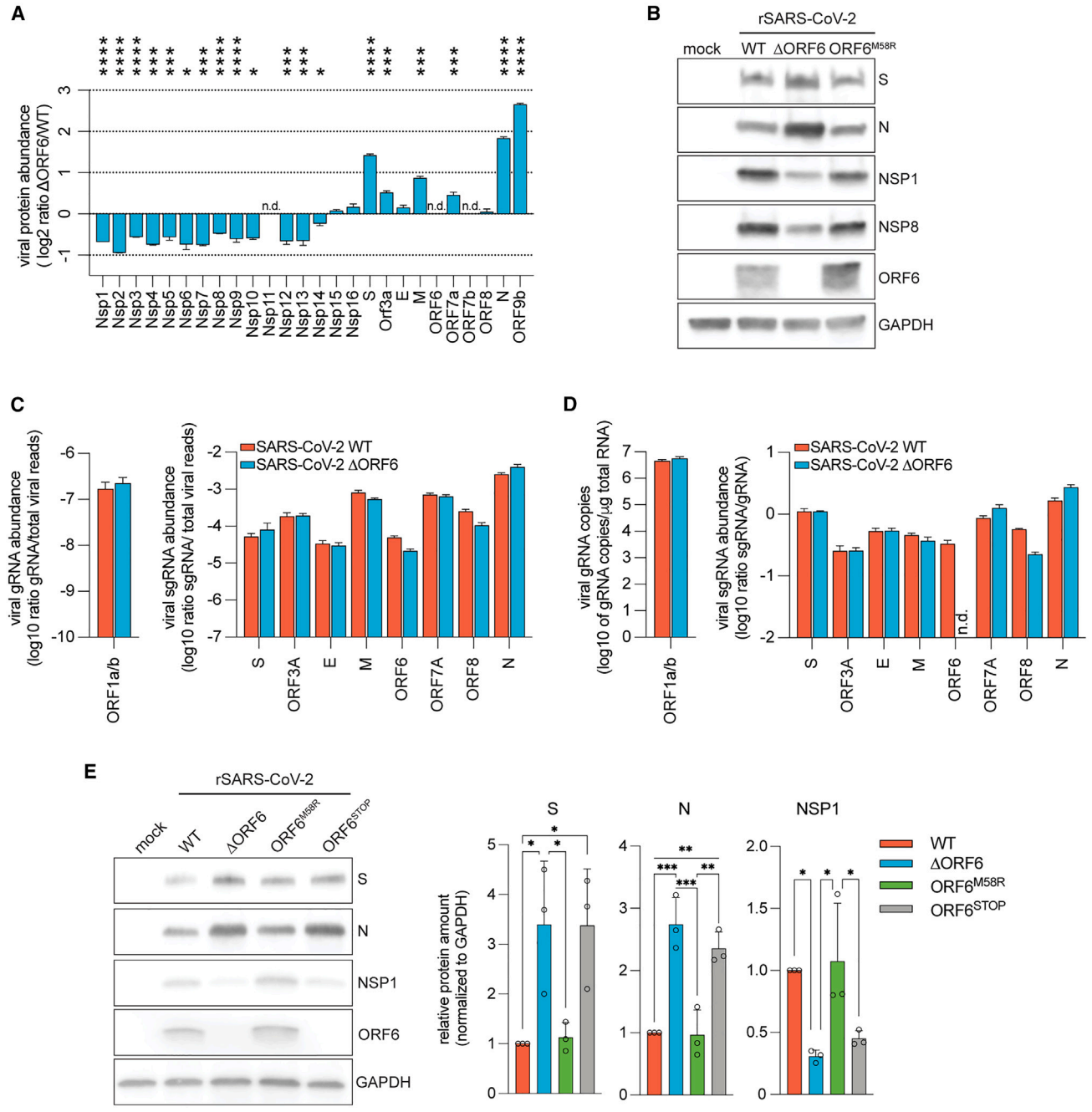

Figure 5. Comparison of viral RNA and protein expression between rSARS-CoV-2 WT and rSARS-CoV-2 ΔORF6

(A) Expression of viral proteins from mass spectrometry abundance proteomics. Graph shows $\log_2$ ratio of summed peptide intensities per viral protein of ΔORF6-infected over WT-infected cells. Data is presented as mean ± SD.

(B) Abundance of the indicated viral proteins assessed by western blot.

(C) Viral gRNA and sgRNA abundance in A549-ACE2 cells infected with indicated viruses. Data are shown as ratio of mapped reads of indicated viral RNA species over the sum of viral reads per sample (n = 3). Data is presented as mean ± SD.

(D) Viral gRNA copy number per μg of total RNA and ratio of indicated sgRNAs over gRNA per sample from samples described in (C) as determined by quantitative real-time-PCR (n = 3). Data is presented as mean ± SD.

(E) Vero E6 cells were infected as indicated, and viral protein expression was assessed by western blot. Quantification of viral protein expression from three biological replicates is shown on the right panels.

Data in (A) were analyzed by two-tailed unpaired Student's multiple t test: ****$p < 0.0001$; ***$p < 0.001$; *$p \leq 0.05$. Data in (C) and (D) were analyzed by Mann-Whitney test with a false detection rate of 5%. Data in (E) were analyzed by ordinary one-way ANOVA using Tukey's multiple comparison test: ***$p < 0.001$; **$p < 0.01$; *$p \leq 0.05$. Graphs were generated with PRISM (version 9).

Please cite this article in press as: Kehrer et al., Impact of SARS-CoV-2 ORF6 and its variant polymorphisms on host responses and viral pathogenesis, Cell Host & Microbe (2023), https://doi.org/10.1016/j.chom.2023.08.003

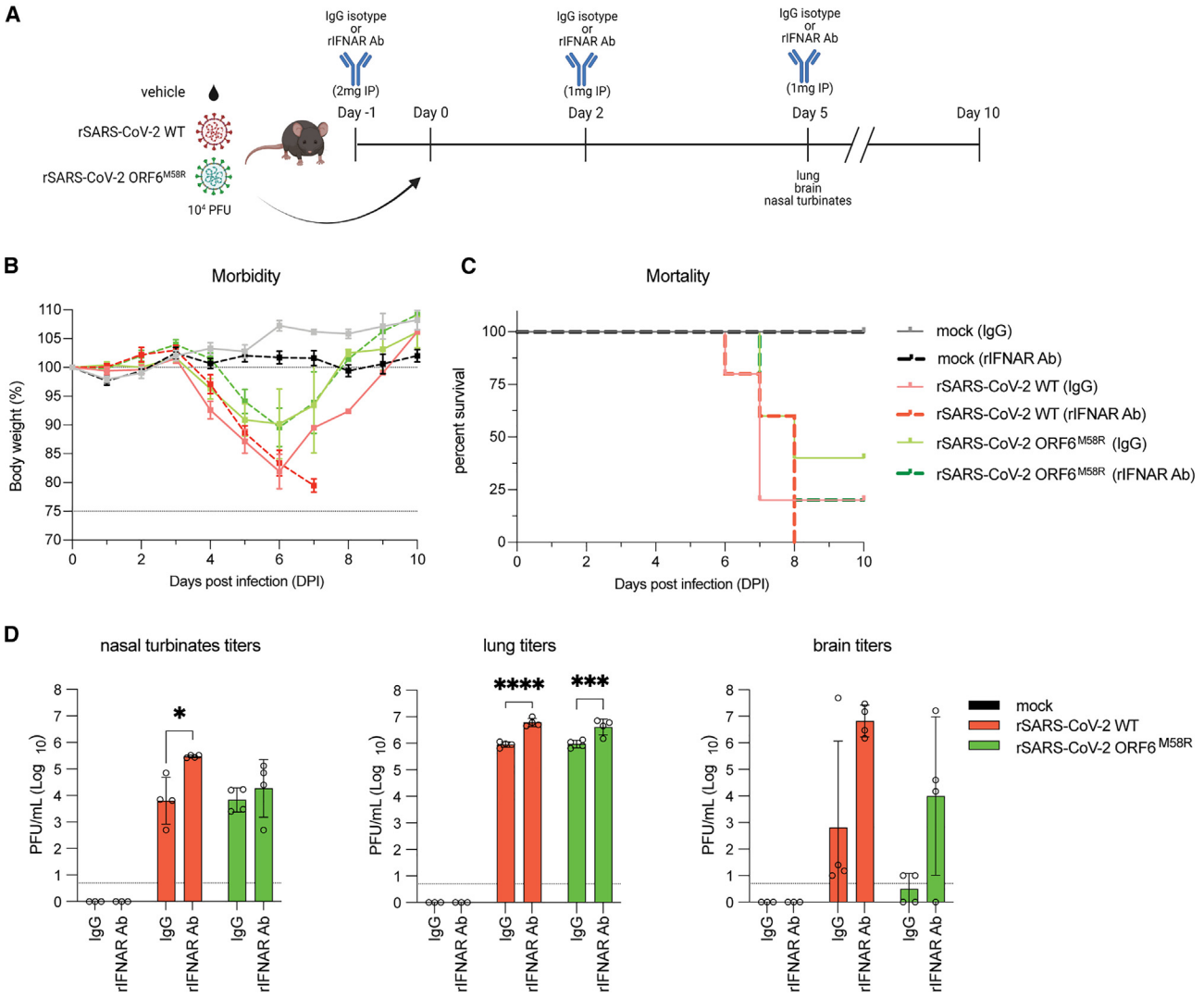

Figure 6. ORF6 contributes to SARS-CoV-2 pathogenesis in K18 human ACE2 transgenic mice

(A) Schematic of the *in vivo* experiment using K18 human ACE2 mice treated with IgG isotype control or rIFNAR-blocking antibodies.

(B) Weight loss data for the duration of the experimentare shown as mean ± SEM.

(C) Mouse survival data for the duration of the experiment.

(D) Nasal turbinates, lung, and brain viral titers at 5 days post-infection. Dashed line indicates the limit of detection for plaque assay (5 PFU/mL). Data is presented as mean ± SD. Data in (D) were analyzed by two-way ANOVA using Tukey's multiple comparison test: ****$p < 0.0001$; ***$p < 0.001$; *$p \leq 0.05$. Graphs were generated with PRISM (version 9).

Interestingly, our work has also revealed a previously unobserved role of ORF6 in the modulation of viral protein expression. We discovered that the relative expression of several ORF1a/b- and sgRNA-derived viral proteins was significantly altered in cells infected with ORF6-deficient SARS-CoV-2 viruses (ΔORF6 and ORF6^{STOP}), to favor expression of several structural and accessory viral genes. At this time, it remains unclear whether this phenomenon is mediated by a direct role of ORF6 on the translational or post-translational regulation of viral gene expression, or a consequence of the altered activity of some of the other viral proteins. However, due to the comparable levels of viral protein expression we observed between the WT and ORF6^{M58R} virus, this phenotype is likely independent of ORF6 functions related to the Nup98-Rae1 complex. Importantly, despite the differences in their NSP1 expression levels, cells infected with both the ORF6-deficient and the ORF6^{M58R} virus clearly showed a reduction in host mRNA nuclear retention, supporting the key role of the direct interaction between ORF6 and the Nup98-Rae1 complex in the block of mRNA export.

Overall, our data strongly suggest that ORF6 is a major SARS-CoV-2 innate immune antagonist. We show that the absence of ORF6, or the introduction of ORF6 loss-of-function mutations, significantly influences the host antiviral responses resulting in SARS-CoV-2 attenuation both *in vitro* in IFN-competent cells, and *in vivo*. In addition, we functionally characterized the ORF6^{D61L} mutation shared by the BA.2, BA.4, and now dominant

Please cite this article in press as: Kehrer et al., Impact of SARS-CoV-2 ORF6 and its variant polymorphisms on host responses and viral pathogenesis, Cell Host & Microbe (2023), https://doi.org/10.1016/j.chom.2023.08.003

CellPress
OPEN ACCESS

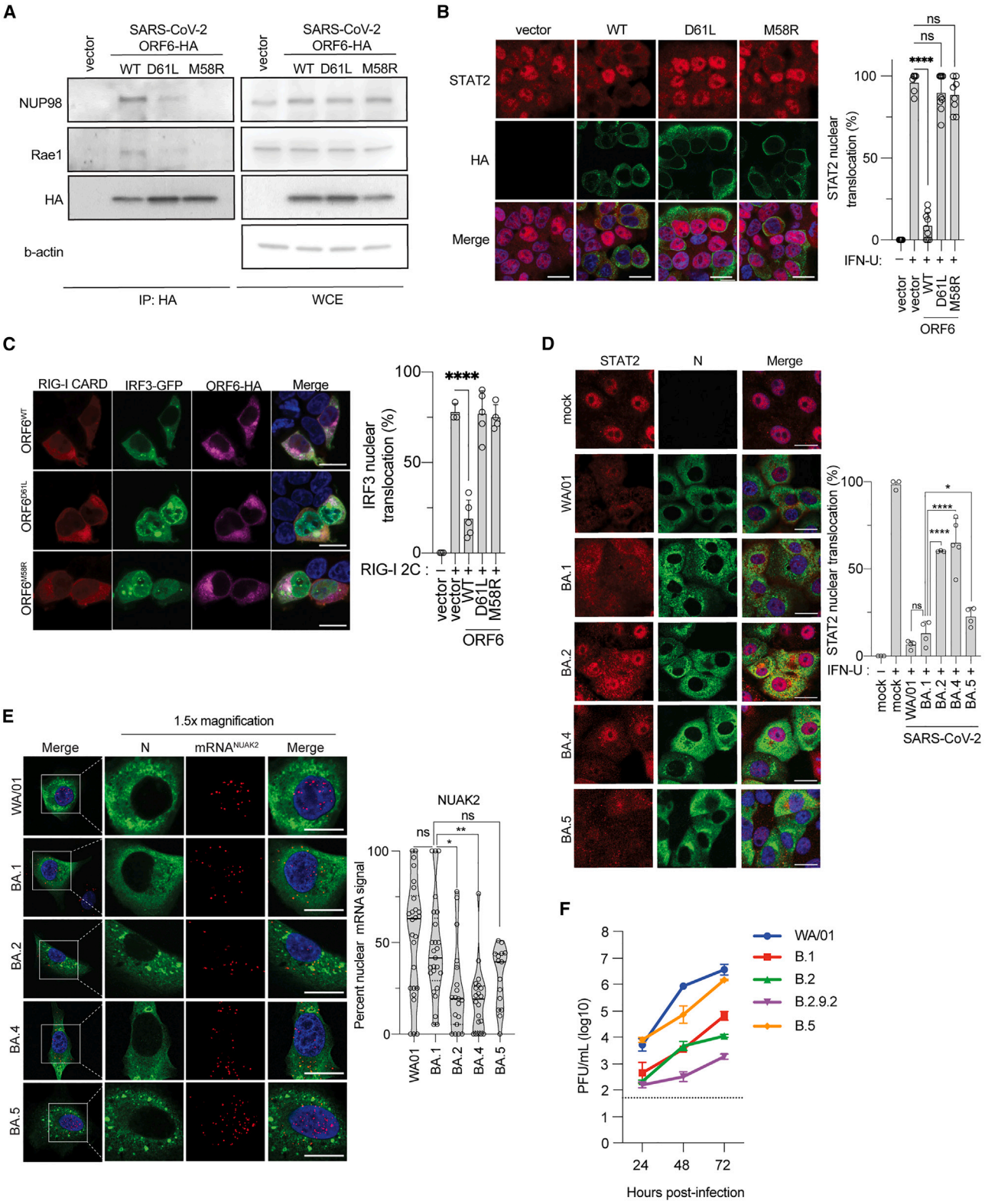

Figure 7. Characterization of the ORF6 D61L mutation

(A) HEK293T cells were transfected with the indicated plasmids and lysates subjected to HA-tag immuno-precipitation as described in STAR Methods (IP:HA, eluate after immunoprecipitation; WCE, whole-cell extract).

(legend continued on next page)

XBB Omicron subvariants, highlighting the importance of genomic surveillance and variant analysis to better understand the mechanisms underlying SARS-CoV-2 evolution, pathogenicity, and immune evasion strategies.

STAR★METHODS

Detailed methods are provided in the online version of this paper and include the following:

- KEY RESOURCES TABLE
- RESOURCE AVAILABILITY
  - Lead contact
  - Materials availability
  - Data and code availability
- EXPERIMENTAL MODEL AND SUBJECT DETAILS
  - Ethics Statement
  - Cell lines
  - Viruses and infections
  - SARS-CoV-2 infection of Syrian Golden Hamsters
  - SARS-CoV-2 infection of K18 human ACE2 transgenic mice
- METHOD DETAILS
  - Plaque assay
  - Western Blot and immunoprecipitation
  - SARS-CoV-2 infection of HTBE cultures (EpiAirway AIR-100 tissues)
  - Luciferase Assay
  - Confocal Microscopy
  - Flow Cytometry
  - Nuclear-cytosolic fractionation
  - SARS-CoV-2 RT-qPCR
  - Immunolabeling with fluorescent in situ hybridization (Immuno-FISH)
  - Immunolabeling with single-molecule RNA-FISH (smRNA-FISH)
  - Mass spectrometry (MS)
  - Immunohistochemistry (IHC)
  - Enzyme-Linked Immunosorbent Assay (ELISA)
- QUANTIFICATION AND STATISTICAL ANALYSIS

SUPPLEMENTAL INFORMATION

Supplemental information can be found online at https://doi.org/10.1016/j.chom.2023.08.003.

ACKNOWLEDGMENTS

We thank all members of the A.G.-S. laboratory for helpful feedback, in particular Teresa Aydillo and Michael Schotsaert for training and support. We thank Randy Albrecht for BSL3 facility support and procedures at the Icahn School of Medicine at Mount Sinai (ISMMS), the staff at the ISMMS Center for Comparative Medicine and Surgery (CCMS) for ABSL3 facility support and Richard Cadagan for technical assistance. We are indebted to the efforts of Mount Sinai Pathogen Surveillance Program (PSP) for collection and sequencing of clinical specimens used to derive viral isolates. Microscopy images were taken at the Microscopy Shared Resource Facility (ISMMS). Animal tissues were processed at the biorepository and Pathology Core (ISMMS) for histology. Bulk RNA sequencing sample libraries were prepared at the Center for Advanced Genomics Technology Facility (ISSMS) directed by Dr. Robert Sebra. This work utilized instruments acquired from NIH SIG grants (S10OD026983 and S10OD030269). Schemes in Figures 4A, 6A, and S4A were created with BioRender.com.

This work was supported by CRIPT (Center for Research on Influenza pathogenesis and Transmission), a NIAID funded Center of Excellence for Influenza Research and Response (CEIRR, contract # 75N93021C00014), and by NIAID grants U19AI142733 and U19AI135972 to A.G.-S.; NCI Seronet grant U54CA260560 to A.G.-S. and B.M.A.F.; and the JPB and OPP foundations and an anonymous philanthropic donor to A.G.-S. This work was also supported by RO1AI161175, RO1AI161363, R21AI173816, Forum Foundation at Texas Biomedical Research Institute, and San Antonio Medical Foundation to L. M.-S.; R01AI151029 to B.R.R.; K99AI163868 to M.B.; NIH grants U19AI171110, U19AI135990, the Excellence in Research Award (ERA) from the Laboratory for Genomics Research (LGR), a collaboration between UCSF, UCB, and GSK (#133122P), and by gifts from QCRG philanthropic donors to N.J.K. This work was supported by the Defense Advanced Research Projects Agency (DARPA) under Cooperative Agreement #HR0011-19-2-0020. The views, opinions, and/or findings contained in this material are those of the authors and should not be interpreted as representing the official views or policies of the Department of Defense or the U.S. Government. S.Y. received funding from Swiss National Foundation (SNF) Postdoc Mobility fellowship (P400PB_199292). A.S.G.-R. received funding from the Marion Alban Mount Sinai Clinical Intelligence Center Scholars Award. The Mount Sinai PSP is supported, in part, by institutional funds.

AUTHOR CONTRIBUTIONS

Conceptualization: L.M. and A.G.-S.; methodology: T.K., A.C., C.Y., S.Y., M.B., N.A.C., E.A.B., P.C., T.C., A.S., A.S.G.-R, B.M.A.F., B.R.R., N.J.K., L.M.-S., A.G.-S., and L.M.; software: M.B., N.A.C., E.A.B., P.C., A.S.G.-R., A.M., H.v.B., B.R.R.; validation: T.K., A.C., M.B., N.A.C., B.R.R., B.M.A.F., N.J.K., L.M.-S, A.G.-S., and L.M.; formal analysis: T.K., A.C., M.B., N.A.C., E.A.B., A.T., T.C., S.A., I.M., and L.M.; investigation: T.K., A.C., C.Y., S.Y., M.B., A.T., R.R., D.F., F.A., I.M., M.R., M.R.U., G.P., B.A., and L.M.; resources: S.J., R.B.R., E.C.V., J.M.F., M.S., B.J.P., M.J.E., D.L.S., E.M.S., H.v.B., and V.S.; visualization: T.K., A.C., M.B., N.A.C., A.T., and L.M.; supervision: S.Y., M.B., N.C., L.Z.-A., B.M.A.F., B.R.R., N.J.K., L.M.-S., A.G.-S., and L.M.; writing – original draft: T.K., A.C., A.G.-S., and L.M.; writing – review & editing: all authors; funding acquisition: N.A.C., B.M.A.F., B.R.R., N.J.K., L.M.-S., and A.G.-S.

(B) HEK293T cells were transfected with the indicated plasmids and then treated with IFN. The subcellular localization of STAT2 was analyzed by immunofluorescence. STAT2 nuclear translocation was quantified from ≥150 cells per condition from two biological replicates. Data is presented as mean ± SD. Scale bar, 20 μm.
(C) HEK293T cells were transfected with the indicated plasmids and then processed for assessment of the subcellular localization of IRF3-GFP. Nuclear translocation of IRF3-GFP in control and ORF6/RIG-I-2CARD double-positive cells was quantified from four fields of view collected from two independent experiments. Data is presented as mean ± SD. Scale bar, 20 μm.
(D) Vero E6 cells were infected with the indicated viruses and then treated with IFN. STAT2 nuclear translocation in infected cells was quantified from ≥150 cells per condition (n = 2).Data is presented as mean ± SD. Scale bar, 20 μm.
(E) A549-ACE2 cells were infected with indicated viruses and processed for smRNA-FISH to determine subcellular localization of NUAK2 transcripts. Transcript localization in infected cells was quantified from ≥15 cells per condition (n = 2). Data are shown as violin plots, solid line marks median, and dashed lines mark quartiles.
(F) Growth curve of indicated viruses in A549-ACE2 cells. Data is presented as mean ± SD.
Data in (B)–(E) were analyzed by ordinary one-way ANOVA using Tukey's multiple comparison test: ****$p < 0.0001$; **$p < 0.01$; *$p \leq 0.05$; ns, not statistically significant. Graphs were generated with PRISM (version 9).

DECLARATION OF INTERESTS

The A.G.-S. laboratory has received research support from Pfizer, Senhwa Biosciences, Kenall Manufacturing, Blade Therapuetics, Avimex, Johnson & Johnson, Dynavax, 7Hills Pharma, Pharmamar, ImmunityBio, Accurius, Nanocomposix, Hexamer, N-fold LLC, Model Medicines, Atea Pharma, Applied Biological Laboratories and Merck, outside of the reported work. A.G.-S. has consulting agreements for the following companies involving cash and/or stock: Castlevax, Amovir, Vivaldi Biosciences, Contrafect, 7Hills Pharma, Avimex, Vaxalto, Pagoda, Accurius, Esperovax, Farmak, Applied Biological Laboratories, Pharmamar, Paratus, CureLab Oncology, CureLab Veterinary, Synairgen and Pfizer, outside of the reported work. A.G.-S. has been an invited speaker in meeting events organized by Seqirus, Janssen, Abbott, and Astrazeneca. A.G.-S. is inventor on patents and patent applications on the use of antivirals and vaccines for the treatment and prevention of virus infections and cancer, owned by ISMMS, New York. C.Y. and L. M.-S. are co-inventors on a patent application directed to reverse genetics approaches to generate recombinant SARS-CoV-2. The Krogan Laboratory has received research support from Vir Biotechnology, F. Hoffmann-La Roche, and Rezo Therapeutics. N.J.K. has previously held financially compensated consulting agreements with the Icahn School of Medicine at Mount Sinai, New York and Twist Bioscience Corp. He currently has financially compensated consulting agreements with Maze Therapeutics, Interline Therapeutics, Rezo Therapeutics, and GEn1E Lifesciences, Inc.. He is on the Board of Directors of Rezo Therapeutics and is a shareholder in Tenaya Therapeutics, Maze Therapeutics, Rezo Therapeutics, and Interline Therapeutics. A.M. is the creator of Omics Bioinformatics and owns all the stocks of this company. ISMMS has filed patent applications relating to SARS-CoV-2 serological assays which list V.S. as co-inventor.

INCLUSION AND DIVERSITY

We support inclusive, diverse, and equitable conduct of research.

Received: January 10, 2023
Revised: July 1, 2023
Accepted: August 7, 2023
Published: September 21, 2023

REFERENCES

1. Blanco-Melo, D., Nilsson-Payant, B.E., Liu, W.C., Uhl, S., Hoagland, D., Møller, R., Jordan, T.X., Oishi, K., Panis, M., Sachs, D., et al. (2020). Imbalanced host response to SARS-CoV-2 drives development of COVID-19. Cell *181*, 1036–1045.e9. https://doi.org/10.1016/j.cell.2020.04.026.
2. Morens, D.M., and Fauci, A.S. (2020). Emerging pandemic diseases: how we got to COVID-19. Cell *182*, 1077–1092. https://doi.org/10.1016/j.cell.2020.08.021.
3. Park, A., and Iwasaki, A. (2020). Type I and Type III interferons - induction, signaling, evasion, and application to combat COVID-19. Cell Host Microbe *27*, 870–878. https://doi.org/10.1016/j.chom.2020.05.008.
4. Boudewijns, R., Thibaut, H.J., Kaptein, S.J.F., Li, R., Vergote, V., Seldeslachts, L., Van Weyenbergh, J., De Keyzer, C., Bervoets, L., Sharma, S., et al. (2020). STAT2 signaling restricts viral dissemination but drives severe pneumonia in SARS-CoV-2 infected hamsters. Nat. Commun. *11*, 5838. https://doi.org/10.1038/s41467-020-19684-y.
5. Bastard, P., Rosen, L.B., Zhang, Q., Michailidis, E., Hoffmann, H.H., Zhang, Y., Dorgham, K., Philippot, Q., Rosain, J., Béziat, V., et al. (2020). Autoantibodies against type I IFNs in patients with life-threatening COVID-19. Science *370*. https://doi.org/10.1126/science.abd4585.
6. Zhang, Q., Bastard, P., Liu, Z., Le Pen, J., Moncada-Velez, M., Chen, J., Ogishi, M., Sabli, I.K.D., Hodeib, S., Korol, C., et al. (2020). Inborn errors of type I IFN immunity in patients with life-threatening COVID-19. Science *370*. https://doi.org/10.1126/science.abd4570.
7. Kehrer, T., García-Sastre, A., and Miorin, L. (2021). Control of innate immune activation by severe acute respiratory syndrome coronavirus 2 and other coronaviruses. J. Interferon Cytokine Res. *41*, 205–219. https://doi.org/10.1089/jir.2021.0060.
8. Miorin, L., Kehrer, T., Sanchez-Aparicio, M.T., Zhang, K., Cohen, P., Patel, R.S., Cupic, A., Makio, T., Mei, M., Moreno, E., et al. (2020). SARS-CoV-2 Orf6 hijacks Nup98 to block STAT nuclear import and antagonize interferon signaling. Proc. Natl. Acad. Sci. USA *117*, 28344–28354. https://doi.org/10.1073/pnas.2016650117.
9. Xia, H., Cao, Z., Xie, X., Zhang, X., Chen, J.Y., Wang, H., Menachery, V.D., Rajsbaum, R., and Shi, P.Y. (2020). Evasion of Type I interferon by SARS-CoV-2. Cell Rep. *33*, 108234. https://doi.org/10.1016/j.celrep.2020.108234.
10. Thoms, M., Buschauer, R., Ameismeier, M., Koepke, L., Denk, T., Hirschenberger, M., Kratzat, H., Hayn, M., Mackens-Kiani, T., Cheng, J., et al. (2020). Structural basis for translational shutdown and immune evasion by the Nsp1 protein of SARS-CoV-2. Science *369*, 1249–1255. https://doi.org/10.1126/science.abc8665.
11. Zhang, K., Miorin, L., Makio, T., Dehghan, I., Gao, S., Xie, Y., Zhong, H., Esparza, M., Kehrer, T., Kumar, A., et al. (2021). Nsp1 protein of SARS-CoV-2 disrupts the mRNA export machinery to inhibit host gene expression. Sci. Adv. *7*. https://doi.org/10.1126/sciadv.abe7386.
12. Finkel, Y., Gluck, A., Nachshon, A., Winkler, R., Fisher, T., Rozman, B., Mizrahi, O., Lubelsky, Y., Zuckerman, B., Slobodin, B., et al. (2021). SARS-CoV-2 uses a multipronged strategy to impede host protein synthesis. Nature *594*, 240–245. https://doi.org/10.1038/s41586-021-03610-3.
13. Huang, C., Lokugamage, K.G., Rozovics, J.M., Narayanan, K., Semler, B.L., and Makino, S. (2011). SARS coronavirus nsp1 protein induces template-dependent endonucleolytic cleavage of mRNAs: viral mRNAs are resistant to nsp1-induced RNA cleavage. PLoS Pathog. *7*, e1002433. https://doi.org/10.1371/journal.ppat.1002433.
14. Burke, J.M., St Clair, L.A., Perera, R., and Parker, R. (2021). SARS-CoV-2 infection triggers widespread host mRNA decay leading to an mRNA export block. RNA *27*, 1318–1329. https://doi.org/10.1261/rna.078923.121.
15. Gordon, D.E., Jang, G.M., Bouhaddou, M., Xu, J., Obernier, K., White, K.M., O'Meara, M.J., Rezelj, V.V., Guo, J.Z., Swaney, D.L., et al. (2020). A SARS-CoV-2 protein interaction map reveals targets for drug repurposing. Nature *583*, 459–468. https://doi.org/10.1038/s41586-020-2286-9.
16. Jiang, H.W., Zhang, H.N., Meng, Q.F., Xie, J., Li, Y., Chen, H., Zheng, Y.X., Wang, X.N., Qi, H., Zhang, J., et al. (2020). SARS-CoV-2 Orf9b suppresses type I interferon responses by targeting TOM70. Cell. Mol. Immunol. *17*, 998–1000. https://doi.org/10.1038/s41423-020-0514-8.
17. Gao, X., Tian, H., Zhu, K., Li, Q., Hao, W., Wang, L., Qin, B., Deng, H., and Cui, S. (2022). Structural basis for Sarbecovirus ORF6 mediated blockage of nucleocytoplasmic transport. Nat. Commun. *13*, 4782. https://doi.org/10.1038/s41467-022-32489-5.
18. Wong, H.T., Cheung, V., and Salamango, D.J. (2022). Decoupling SARS-CoV-2 ORF6 localization and interferon antagonism. J. Cell Sci. *135*. https://doi.org/10.1242/jcs.259666.
19. Li, T., Wen, Y., Guo, H., Yang, T., Yang, H., and Ji, X. (2021). Molecular mechanism of SARS-CoVs Orf6 targeting the Rae1-Nup98 complex to compete with mRNA nuclear export. Front. Mol. Biosci. *8*, 813248. https://doi.org/10.3389/fmolb.2021.813248.
20. Addetia, A., Lieberman, N.A.P., Phung, Q., Hsiang, T.Y., Xie, H., Roychoudhury, P., Shrestha, L., Loprieno, M.A., Huang, M.L., Gale, M., Jr., et al. (2021). SARS-CoV-2 ORF6 disrupts bidirectional nucleocytoplasmic transport through interactions with Rae1 and Nup98. mBio *12*. https://doi.org/10.1128/mBio.00065-21.
21. Hall, R., Guedán, A., Yap, M.W., Young, G.R., Harvey, R., Stoye, J.P., and Bishop, K.N. (2022). SARS-CoV-2 ORF6 disrupts innate immune signalling by inhibiting cellular mRNA export. PLoS Pathog. *18*, e1010349. https://doi.org/10.1371/journal.ppat.1010349.
22. Davies, N.G., Abbott, S., Barnard, R.C., Jarvis, C.I., Kucharski, A.J., Munday, J.D., Pearson, C.A.B., Russell, T.W., Tully, D.C., Washburne, A.D., et al. (2021). Estimated transmissibility and impact of SARS-CoV-2 lineage B.1.1.7 in England. Science *372*. https://doi.org/10.1126/science.abg3055.
23. Tegally, H., Moir, M., Everatt, J., Giovanetti, M., Scheepers, C., Wilkinson, E., Subramoney, K., Makatini, Z., Moyo, S., Amoako, D.G., et al. (2022). Emergence of SARS-CoV-2 Omicron lineages BA.4 and BA.5 in South

Africa. Nat. Med. *28*, 1785–1790. https://doi.org/10.1038/s41591-022-01911-2.

24. Thorne, L.G., Bouhaddou, M., Reuschl, A.K., Zuliani-Alvarez, L., Polacco, B., Pelin, A., Batra, J., Whelan, M.V.X., Hosmillo, M., Fossati, A., et al. (2022). Evolution of enhanced innate immune evasion by SARS-CoV-2. Nature *602*, 487–495. https://doi.org/10.1038/s41586-021-04352-y.
25. Ye, C., Chiem, K., Park, J.G., Oladunni, F., Platt, R.N., 2nd, Anderson, T., Almazan, F., de la Torre, J.C., and Martinez-Sobrido, L. (2020). Rescue of SARS-CoV-2 from a single bacterial artificial chromosome. mBio *11*. https://doi.org/10.1128/mBio.02168-20.
26. Silvas, J.A., Vasquez, D.M., Park, J.G., Chiem, K., Allué-Guardia, A., Garcia-Vilanova, A., Platt, R.N., Miorin, L., Kehrer, T., Cupic, A., et al. (2021). Contribution of SARS-CoV-2 accessory proteins to viral pathogenicity in K18 human ACE2 transgenic mice. J. Virol. *95*, e0040221. https://doi.org/10.1128/JVI.00402-21.
27. Chiem, K., Ye, C., and Martinez-Sobrido, L. (2020). Generation of recombinant SARS-CoV-2 using a bacterial artificial chromosome. Curr. Protoc. Microbiol. *59*, e126. https://doi.org/10.1002/cpmc.126.
28. Kimura, I., Konno, Y., Uriu, K., Hopfensperger, K., Sauter, D., Nakagawa, S., and Sato, K. (2021). Sarbecovirus ORF6 proteins hamper induction of interferon signaling. Cell Rep. *34*, 108916. https://doi.org/10.1016/j.celrep.2021.108916.
29. Foy, E., Li, K., Wang, C., Sumpter, R., Jr., Ikeda, M., Lemon, S.M., and Gale, M., Jr. (2003). Regulation of interferon regulatory factor-3 by the hepatitis C virus serine protease. Science *300*, 1145–1148. https://doi.org/10.1126/science.1082604.
30. Shi, M., Cho, H., Inn, K.S., Yang, A., Zhao, Z., Liang, Q., Versteeg, G.A., Amini-Bavil-Olyaee, S., Wong, L.Y., Zlokovic, B.V., et al. (2014). Negative regulation of NF-κB activity by brain-specific TRIpartite Motif protein 9. Nat. Commun. *5*, 4820. https://doi.org/10.1038/ncomms5820.
31. Gruber, A.D., Firsching, T.C., Trimpert, J., and Dietert, K. (2022). Hamster models of COVID-19 pneumonia reviewed: how human can they be? Vet. Pathol. *59*, 528–545. https://doi.org/10.1177/03009858211057197.
32. Chong, Z., Karl, C.E., Halfmann, P.J., Kawaoka, Y., Winkler, E.S., Keeler, S.P., Holtzman, M.J., Yu, J., and Diamond, M.S. (2022). Nasally delivered interferon-lambda protects mice against infection by SARS-CoV-2 variants including Omicron. Cell Rep. *39*, 110799. https://doi.org/10.1016/j.celrep.2022.110799.
33. Schneider, W.M., Chevillotte, M.D., and Rice, C.M. (2014). Interferon-stimulated genes: a complex web of host defenses. Annu. Rev. Immunol. *32*, 513–545. https://doi.org/10.1146/annurev-immunol-032713-120231.
34. Hadjadj, J., Yatim, N., Barnabei, L., Corneau, A., Boussier, J., Smith, N., Péré, H., Charbit, B., Bondet, V., Chenevier-Gobeaux, C., et al. (2020). Impaired type I interferon activity and inflammatory responses in severe COVID-19 patients. Science *369*, 718–724. https://doi.org/10.1126/science.abc6027.
35. Liang, P., Zhang, H., Wang, G., Li, S., Cong, S., Luo, Y., and Zhang, B. (2013). KPNB1, XPO7 and IPO8 mediate the translocation of NF-κB/p65 into the nucleus. Traffic *14*, 1132–1143. https://doi.org/10.1111/tra.12097.
36. De Jesús-González, L.A., Palacios-Rápalo, S., Reyes-Ruiz, J.M., Osuna-Ramos, J.F., Cordero-Rivera, C.D., Farfan-Morales, C.N., Gutiérrez-Escolano, A.L., and Del Ángel, R.M. (2021). The nuclear pore complex is a key target of viral proteases to promote viral replication. Viruses *13*. https://doi.org/10.3390/v13040706.
37. Sajidah, E.S., Lim, K., and Wong, R.W. (2021). How SARS-CoV-2 and other viruses build an invasion route to hijack the Host Nucleocytoplasmic Trafficking System. Cells *10*. https://doi.org/10.3390/cells10061424.
38. Yarbrough, M.L., Mata, M.A., Sakthivel, R., and Fontoura, B.M. (2014). Viral subversion of nucleocytoplasmic trafficking. Traffic *15*, 127–140. https://doi.org/10.1111/tra.12137.
39. Faria, P.A., Chakraborty, P., Levay, A., Barber, G.N., Ezelle, H.J., Enninga, J., Arana, C., van Deursen, J., and Fontoura, B.M. (2005). VSV disrupts the Rae1/mrnp41 mRNA nuclear export pathway. Mol. Cell *17*, 93–102. https://doi.org/10.1016/j.molcel.2004.11.023.
40. Gong, D., Kim, Y.H., Xiao, Y., Du, Y., Xie, Y., Lee, K.K., Feng, J., Farhat, N., Zhao, D., Shu, S., et al. (2016). A herpesvirus protein selectively inhibits cellular mRNA nuclear export. Cell Host Microbe *20*, 642–653. https://doi.org/10.1016/j.chom.2016.10.004.
41. Quan, B., Seo, H.S., Blobel, G., and Ren, Y. (2014). Vesiculoviral matrix (M) protein occupies nucleic acid binding site at nucleoporin pair (Rae1 * Nup98). Proc. Natl. Acad. Sci. USA *111*, 9127–9132. https://doi.org/10.1073/pnas.1409076111.
42. Feng, H., Tian, H., Wang, Y., Zhang, Q., Lin, N., Liu, S., Yu, Y., Deng, H., and Gao, P. (2020). Molecular mechanism underlying selective inhibition of mRNA nuclear export by herpesvirus protein ORF10. Proc. Natl. Acad. Sci. USA *117*, 26719–26727. https://doi.org/10.1073/pnas.2007774117.
43. Kim, S.J., Fernandez-Martinez, J., Nudelman, I., Shi, Y., Zhang, W., Raveh, B., Herricks, T., Slaughter, B.D., Hogan, J.A., Upla, P., et al. (2018). Integrative structure and functional anatomy of a nuclear pore complex. Nature *555*, 475–482. https://doi.org/10.1038/nature26003.
44. Stewart, M. (2010). Nuclear export of mRNA. Trends Biochem. Sci. *35*, 609–617. https://doi.org/10.1016/j.tibs.2010.07.001.
45. Bouhaddou, M., Reuschl, A.-K., Polacco, B.J., Thorne, L.G., Ummadi, M.R., Ye, C., Rosales, R., Pelin, A., Batra, J., Jang, G.M., et al. (2023). SARS-CoV-2 variants evolve convergent strategies to remodel the host response. Cell *186*. https://doi.org/10.1016/j.cell.2023.08.026.
46. Uraki, R., Halfmann, P.J., Iida, S., Yamayoshi, S., Furusawa, Y., Kiso, M., Ito, M., Iwatsuki-Horimoto, K., Mine, S., Kuroda, M., et al. (2022). Characterization of SARS-CoV-2 omicron BA.4 and BA.5 isolates in rodents. Nature *612*, 540–545. https://doi.org/10.1038/s41586-022-05482-7.
47. Miorin, L., Mire, C.E., Ranjbar, S., Hume, A.J., Huang, J., Crossland, N.A., White, K.M., Laporte, M., Kehrer, T., Haridas, V., et al. (2022). The oral drug nitazoxanide restricts SARS-CoV-2 infection and attenuates disease pathogenesis in Syrian hamsters. Preprint at bioRxiv. https://doi.org/10.1101/2022.02.08.479634.
48. Dagotto, G., Mercado, N.B., Martinez, D.R., Hou, Y.J., Nkolola, J.P., Carnahan, R.H., Crowe, J.E., Jr., Baric, R.S., and Barouch, D.H. (2021). Comparison of subgenomic and total RNA in SARS-CoV-2 challenged rhesus macaques. J. Virol. *95*. https://doi.org/10.1128/JVI.02370-20.
49. Escalante, C.R., Nistal-Villán, E., Shen, L., García-Sastre, A., and Aggarwal, A.K. (2007). Structure of IRF-3 bound to the PRDIII-I regulatory element of the human interferon-beta enhancer. Mol. Cell *26*, 703–716. https://doi.org/10.1016/j.molcel.2007.04.022.
50. Sánchez-Aparicio, M.T., Ayllón, J., Leo-Macias, A., Wolff, T., and García-Sastre, A. (2017). Subcellular localizations of RIG-I, TRIM25, and MAVS complexes. J. Virol. *91*. https://doi.org/10.1128/JVI.01155-16.
51. Ashour, J., Morrison, J., Laurent-Rolle, M., Belicha-Villanueva, A., Plumlee, C.R., Bernal-Rubio, D., Williams, K.L., Harris, E., Fernandez-Sesma, A., Schindler, C., et al. (2010). Mouse STAT2 restricts early dengue virus replication. Cell Host Microbe *8*, 410–421. https://doi.org/10.1016/j.chom.2010.10.007.
52. Versteeg, G.A., Rajsbaum, R., Sánchez-Aparicio, M.T., Maestre, A.M., Valdiviezo, J., Shi, M., Inn, K.S., Fernandez-Sesma, A., Jung, J., and García-Sastre, A. (2013). The E3-ligase TRIM family of proteins regulates signaling pathways triggered by innate immune pattern-recognition receptors. Immunity *38*, 384–398. https://doi.org/10.1016/j.immuni.2012.11.013.
53. Manganaro, L., de Castro, E., Maestre, A.M., Olivieri, K., García-Sastre, A., Fernandez-Sesma, A., and Simon, V. (2015). HIV Vpu interferes with NF-κB activity but not with Interferon Regulatory Factor 3. J. Virol. *89*, 9781–9790. https://doi.org/10.1128/JVI.01596-15.
54. Perez-Riverol, Y., Bai, J., Bandla, C., García-Seisdedos, D., Hewapathirana, S., Kamatchinathan, S., Kundu, D.J., Prakash, A., Frericks-Zipper, A., Eisenacher, M., et al. (2022). The PRIDE database resources in 2022: a hub for mass spectrometry-based proteomics evidences. Nucleic Acids Res. *50*, D543–D552. https://doi.org/10.1093/nar/gkab1038.
55. Daniloski, Z., Jordan, T.X., Wessels, H.H., Hoagland, D.A., Kasela, S., Legut, M., Maniatis, S., Mimitou, E.P., Lu, L., Geller, E., et al. (2021).

Identification of required host factors for SARS-CoV-2 infection in human cells. Cell *184*, 92–105.e16. https://doi.org/10.1016/j.cell.2020.10.030.

56. Escalera, A., Gonzalez-Reiche, A.S., Aslam, S., Mena, I., Laporte, M., Pearl, R.L., Fossati, A., Rathnasinghe, R., Alshammary, H., van de Guchte, A., et al. (2022). Mutations in SARS-CoV-2 variants of concern link to increased spike cleavage and virus transmission. Cell Host Microbe *30*, 373–387.e7. https://doi.org/10.1016/j.chom.2022.01.006.
57. Gonzalez-Reiche, A.S., Hernandez, M.M., Sullivan, M.J., Ciferri, B., Alshammary, H., Obla, A., Fabre, S., Kleiner, G., Polanco, J., Khan, Z., et al. (2020). Introductions and early spread of SARS-CoV-2 in the New York City area. Science *369*, 297–301. https://doi.org/10.1126/science.abc1917.
58. Amanat, F., White, K.M., Miorin, L., Strohmeier, S., McMahon, M., Meade, P., Liu, W.C., Albrecht, R.A., Simon, V., Martinez-Sobrido, L., et al. (2020). An in vitro microneutralization assay for SARS-CoV-2 serology and drug screening. Curr. Protoc. Microbiol. *58*, e108. https://doi.org/10.1002/cpmc.108.
59. Pfaffl, M.W. (2001). A new mathematical model for relative quantification in real-time RT-PCR. Nucleic Acids Res. *29*, e45. https://doi.org/10.1093/nar/29.9.e45.
60. Mor, A., White, A., Zhang, K., Thompson, M., Esparza, M., Muñoz-Moreno, R., Koide, K., Lynch, K.W., García-Sastre, A., and Fontoura, B.M. (2016). Influenza virus mRNA trafficking through host nuclear speckles. Nat. Microbiol. *1*, 16069. https://doi.org/10.1038/nmicrobiol.2016.69.
61. Parker, M.D., Lindsey, B.B., Leary, S., Gaudieri, S., Chopra, A., Wyles, M., Angyal, A., Green, L.R., Parsons, P., Tucker, R.M., et al. (2021). Subgenomic RNA identification in SARS-CoV-2 genomic sequencing data. Genome Res. *31*, 645–658. https://doi.org/10.1101/gr.268110.120.

Please cite this article in press as: Kehrer et al., Impact of SARS-CoV-2 ORF6 and its variant polymorphisms on host responses and viral pathogenesis, Cell Host & Microbe (2023), https://doi.org/10.1016/j.chom.2023.08.003

STAR★METHODS

KEY RESOURCES TABLE

REAGENT or RESOURCE	SOURCE	IDENTIFIER
Antibodies		
Mouse monoclonal anti-SARS-CoV-1/2 N (Immunoblotting, Immunostaining, Immunofluorescence microscopy)	Center for Therapeutic Antibody Development (CTAD), Icahn School of Medicine at Mount Sinai	Cat#1C7C7
Sheep polyclonal anti-SARS-CoV-2 ORF6 (Immunoblotting)	MRC PPU Reagents and Services	Cat#DA087
Rabbit polyclonal anti-Rae1 (Immunoblotting)	Thermo Fisher	Cat# PA5-93166; RRID:AB_2806650
Rat monoclonal anti-NUP98 (Immunoblotting, Immunoprecipitation)	Abcam	Cat#ab50610; RRID:AB_2894964
IgG isotype control (Immunoprecipitation)	Cell Signaling Technology	Cat#3900S; RRID:AB_1550038
Rabbit monoclonal anti-phospho-STAT1 (Immunoblotting, Immunohistochemistry, Immunofluorescence microscopy)	Cell Signaling Technology	Cat#9167S; RRID:AB_561284
Mouse monoclonal anti-STAT1 (Immunoblotting)	Santa Cruz	Cat#sc-417; RRID: AB_675902
Rabbit monoclonal anti-phospho-STAT2 (Immunoblotting)	Cell Signaling Technology	Cat#88410S; RRID:AB_2800123
Rabbit polyclonal anti-STAT2 (Immunoblotting, Immunofluorescence microscopy)	Santa Cruz	Cat#sc-476; RRID:AB_632437
Rabbit monoclonal anti-GAPDH conjugated with HRP (Immunoblotting)	Cell Signaling Technology	Cat#3683S; RRID:AB_1642205
Rabbit monoclonal anti-phospho-IRF3 (Immunoblotting, Immunofluorescence microscopy)	Cell Signaling Technology	Cat#4947S; RRID:AB_823547
Rabbit monoclonal anti-IRF3 (Immunoblotting)	Cell Signaling Technology	Cat#11904S; RRID:AB_2722521
Rabbit monoclonal anti-phospho-p65 (Immunoblotting)	Cell Signaling Technology	Cat#3033S; RRID:AB_331284
Rabbit monoclonal anti-p65 (Immunoblotting, Immunofluorescence microscopy)	Cell Signaling Technology	Cat#8242S; RRID:AB_10859369
Mouse monoclonal anti-SARS-CoV-1/2 Spike (Immunoblotting)	Sigma Aldrich	Cat#ZMS1076; RRID:AB_2893440
Rabbit polyclonal anti-SARS-CoV-2 Nsp1 (Immunoblotting)	Genetex	Cat#GTX135612; RRID:AB_2887504
Mouse monoclonal anti-SARS-CoV-2 Nsp8 (Immunoblotting)	Genetex	Cat#GTX632696; RRID:AB_2888329
Mouse monoclonal anti-FLAG (Immunoblotting)	Sigma Aldrich	Cat#F1804; RRID:AB_262044
Mouse monoclonal anti-HA (Immunoblotting, Immunofluorescence microscopy)	Cell Signaling Technology	Cat#2367S; RRID:AB_10691311
Rabbit monoclonal anti-HA (Immunofluorescence microscopy)	Cell Signaling Technology	Cat#3724S; RRID:AB_1549585
Mouse monoclonal anti-HA conjugated with HRP (Immunoblotting)	Cell Signaling Technology	Cat#2999S; RRID:AB_1264166
Rabbit monoclonal anti-SARS-CoV-2 Spike (S1) (Immunohistochemistry)	Cell Signaling Technology	Cat#99423S

(*Continued on next page*)

Please cite this article in press as: Kehrer et al., Impact of SARS-CoV-2 ORF6 and its variant polymorphisms on host responses and viral pathogenesis, Cell Host & Microbe (2023), https://doi.org/10.1016/j.chom.2023.08.003

Continued

REAGENT or RESOURCE	SOURCE	IDENTIFIER
Mouse monoclonal anti-MxA (Immunohistochemistry)	EMD Millipore	Cat#MABF938; RRID:AB_2885181
Mouse monoclonal anti-Ki67 (Immunohistochemistry)	Agilent	Cat#M724001-2; RRID:AB_2142367
Goat polyclonal anti-mouse IgG conjugated with HRP (Immunoblotting)	Kindle Biosciences	Cat#1005; RRID:AB_2800463
Goat polyclonal anti-rabbit IgG conjugated with HRP (Immunoblotting)	Kindle Biosciences	Cat#1006; RRID:AB_2800464
Goat polyclonal anti-rat IgG conjugated with HRP (Immunoblotting)	Invitrogen	Cat#31470; RRID:AB_228356
Donkey polyclonal anti-sheep IgG conjugated with HRP (Immunoblotting)	Invitrogen	Cat#A16041; RRID:AB_2534715
Goat polyclonal anti-mouse IgG conjugated with HRP(Immunostaining)	Abcam	Cat#ab6823; RRID:AB_955395
Goat polyclonal anti-golden syrian hamster IgG conjugated with HRP (ELISA)	Abcam	Cat#ab6892; RRID:AB_955427
Goat anti-rabbit HRP-polymer (Immunohistochemistry)	Vector Laboratories	Cat#MP-7451; RRID:AB_2631198
Goat anti-mouse HRP-polymer (Immunohistochemistry)	Vector Laboratories	Cat#MP-7452; RRID:AB_2744550
Donkey anti-mouse IgG conjugated with AlexaFluor488 (Immunofluorescence microscopy)	Invitrogen	Cat#A21202; RRID:AB_141607
Donkey anti-rabbit IgG conjugated with AlexaFluor594 (Immunofluorescence microscopy)	Invitrogen	Cat#A21207; RRID:AB_141637
Donkey anti-mouse IgG conjugated with AlexaFluor647 (Immunofluorescence microscopy)	Invitrogen	Cat#A31571; RRID:AB_162542
Donkey anti-mouse IgG conjugated with AlexaFluor594 (Immunofluorescence microscopy)	Invitrogen	Cat#A11005; RRID:AB_141372
Anti-mouse IFNAR-1 MAR1-5A3 - Purified *in vivo* PLATINUM Functional Grade (*in vivo*)	Leinco Technologies, Inc.	Product No.: I-1188; RRID:AB_2830518
Mouse IgG1 Isotype Control (Clone HKSP) – Purified in vivo PLATINUM Functional grade (*in vivo*)	Leinco Technologies, Inc.	Product No.: M1411; RRID:AB_2831344
Bacterial and virus strains		
Recombinant SARS-COV-2	Silvas et al.[26]	N/A
Recombinant SARS-COV-2 ΔORF6	Silvas et al.[26]	N/A
Recombinant SARS-COV-2 ORF6M58R	This paper	N/A
Recombinant SARS-COV-2 ORF6STOP	This paper	N/A
SARS-CoV-2 isolate USA-WA1/2020	BEI resources	Cat#NR-52281
SARS-CoV-2 isolate USA/NY-MSHSPSP-PV44488/2021 (Omicron BA.1)	Mount Sinai Pathogen Surveillance Program	PV44488
SARS-CoV-2 isolate USA/NY-MSHSPSP-PV56107/2022 (Omicron BA.2)	Mount Sinai Pathogen Surveillance Program	PV56107
SARS-CoV-2 isolate USA/NY-MSHSPSP-PV56159/2022 (Omicron BA.2.9.2)	Mount Sinai Pathogen Surveillance Program	PV56159
SARS-CoV-2 isolate USA/MD-HP30386/2022 (Omicron BA.4)	BEI resources	Cat#NR-56803
SARS-CoV-2 isolate USA/NY-MSHSPSP-PV58128/2022 (Omicron BA.5)	Mount Sinai Pathogen Surveillance Program	PV58128
Stellar™ Competent Cells	Takara Bio	Cat#636763

(*Continued on next page*)

Please cite this article in press as: Kehrer et al., Impact of SARS-CoV-2 ORF6 and its variant polymorphisms on host responses and viral pathogenesis, Cell Host & Microbe (2023), https://doi.org/10.1016/j.chom.2023.08.003

Continued

REAGENT or RESOURCE	SOURCE	IDENTIFIER
Chemicals, peptides, and recombinant proteins		
DAPI (Immunofluorescence microscopy)	Sigma Aldrich	Cat#MBD001
DAPI (Immunohistochemistry)	Akoya Biosciences	Cat#FP1490
Recombinant SARS-CoV-2 Spike (S) protein	Sino Biological	Cat#40589-V08H4
Universal Type I Interferon Alpha	PBL Assay Science	Cat#11200-2
TNF-alpha	Bio-Techne	Cat#210-TA-020/CF
Critical commercial assays		
MinION flow cell (R.9.4.1)	Oxford nanopore	Cat#FLO-MIN106D
Nextera XT DNA Sample Preparation kit	Illumina	FC-131
Native barcoding expansion 1-12/13-24	Oxford nanopore	Cat#EXP-NBD114
Dual-Luciferase Assay System	Promega	Cat#E1960
TaqMan Universal Master Mix II with UNG	Applied Biosystems	Cat#4440038
ViewRNA Cell Plus Assay Kit	Invitrogen	Cat#88-19000-99
SMART-Seq v4 PLUS Kit	Takara Bio	Cat#R400752
NextSeq 500/550 Mid Output Kit v2.5 (300 Cycles)	Illumina	Cat#20024905
AlexaFluor488-antibody labeling kit	Invitrogen	Cat#A20181
RiboPure kitKit	Invitrogen	Cat#AM1924
miRNeasy mini kit	QIAGEN	Cat#217004
Deposited data		
RNA sequencing data	This paper	PRIDE: PXD036821
Proteomics data	This paper	GEO: GSE215433
Experimental models: Cell lines		
Human: A549-ACE2	Miorin et al.[47]	N/A
Human: HEK293-T	ATCC	Cat#CRL-3216; RRID:CVCL_0063
African Green Monkey: Vero E6	ATCC	Cat#CRL-1586; RRID:CVCL_0574
African Green Monkey: TMPRSS2-Vero E6	BPS Bioscience	Cat#78081
Golden Syrian Hamster: BHK-21	ATCC	Cat#CCL-10; RRID:CVCL_1915
Mouse: L-929	ATCC	Cat#CCL-1; RRID:CVCL_0462
EpiAirway, 3D Respiratory Epithelial Human MicroTissues	Mattek	Cat#AIR-100
Experimental models: Organisms/strains		
Golden Syrian Hamster	Envigo	Strain: HsdHan®:AURA
Mouse	The Jackson Laboratory	Strain: B6.Cg-Tg(K18-ACE2)2Prlmn/J; RRID:MGI:6389236
Oligonucleotides		
GAPDH primer/probe mix	ThermoFisher	Cat#Hs02786624_g1
MALAT-1 primer/probe mix	ThermoFisher	Cat#Hs00273907_s1
NUAK2 primer/probe mix	ThermoFisher	Cat#Hs00388292_m1
NFKB primer/probe mix	ThermoFisher	Cat#Hs00765730_m1
CXCL3 primer/probe mix	ThermoFisher	Cat#Hs00171061_m1
IRF1 primer/probe mix	ThermoFisher	Cat#Hs00971965_m1
SARS-CoV-2 ORF1ab-forward GGCCAATTCTGCTGTCAAATTA	Dagotto et al.[48]	N/A
SARS-CoV-2 ORF1ab-reverse CAGTGCAAGCAGTTTGTGTAG	Dagotto et al.[48]	N/A
SARS-CoV-2 ORF1ab-probe FAM-ACAGATGTCTTGTGCTGCCGGTA-BHQ1	Dagotto et al.[48]	N/A

(*Continued on next page*)

Please cite this article in press as: Kehrer et al., Impact of SARS-CoV-2 ORF6 and its variant polymorphisms on host responses and viral pathogenesis, Cell Host & Microbe (2023), https://doi.org/10.1016/j.chom.2023.08.003

Continued

REAGENT or RESOURCE	SOURCE	IDENTIFIER
SARS-CoV-2 Leader-forward CGATCTCTTGTAGATCTGTTCTC	Dagotto et al.[48]	N/A
SARS-CoV-2 NSP1 (set 1)-reverse CAGGGACAAGGCTCTCCAT	This paper	N/A
SARS-CoV-2 NSP1 (set 2)-reverse CGTGTGTTTTCTCGTTGAAAC	This paper	N/A
SARS-CoV-2 S (set 1)-reverse ACCAAGTAACATTGGAAAAGAAAGG	This paper	N/A
SARS-CoV-2 S (set 2)-reverse CTGAGTTGAATGTAAAACTGAGG	This paper	N/A
SARS-CoV-2 ORF3a (set 1)-reverse GCAACGCCAACAATAAGCC	This paper	N/A
SARS-CoV-2 ORF3a (set 2)-reverse GAGGGTTATGATTTTGGAAGCG	This paper	N/A
SARS-CoV-2 E (set 1)-reverse CAGATTTTTAACACGAGAGTAAACG	This paper	N/A
SARS-CoV-2 E (set 2)-reverse CTCACGTTAACAATATTGCAGC	This paper	N/A
SARS-CoV-2 M (set 1)-reverse GGCAAATTGTAGAAGACAAATCCATG	This paper	N/A
SARS-CoV-2 M (set 2)-reverse TGGCCATAACAGCCAGAGG	This paper	N/A
SARS-CoV-2 ORF6 (set 1)-reverse ACCTGAAAGTCAACGAGATGAAAC	This paper	N/A
SARS-CoV-2 ORF6 (set 2)-reverse GTCAACGAGATGAAACATCTG	This paper	N/A
SARS-CoV-2 ORF7a (set 1)-reverse GTTATCAGCTAGAGGATGAAATGGTG	This paper	N/A
SARS-CoV-2 ORF7a (set 2)-reverse GCAAATTGAGTGCTAAAGCAAGTC	This paper	N/A
SARS-CoV-2 ORF8 (set 1)-reverse GGTGCTGATTTTCTAGCTCC	This paper	N/A
SARS-CoV-2 ORF8 (set 2)-reverse CCAGCCTCATCCACGC	This paper	N/A
SARS-CoV-2 N (set 1)-reverse TTGTCCTCGAGGGAATTTAAGG	This paper	N/A
SARS-CoV-2 N (set 2)-reverse CAGTATTATTGGGTAAACCTTGG	This paper	N/A
rSARS-CoV-2 ORF6^{M58R}-forward CTCAATTAGATGAAGAGCAACC ACGGGAGATTGATTAAACG	This paper	N/A
rSARS-CoV-2 ORF6^{M58R}-reverse TCATGTTCGTTTAATCAATCTCC CGTGGTTGCTCTTCATCT	This paper	N/A
rSARS-CoV-2 ORF6^{STOP}-forward GACTTTCAGGTTACTATAGCAGA GATATTACTAATTATTTAAAGGAC TTTTAAAGTTTCCATTTGGAAT	This paper	N/A
rSARS-CoV-2 ORF6^{STOP}-reverse ATCTCTGCTATAGTAACCTGAAAG TCAACGAGATGTTATTACTGTTGTC ACTTACTGTACAAGCAAAGC	This paper	N/A

(*Continued on next page*)

Please cite this article in press as: Kehrer et al., Impact of SARS-CoV-2 ORF6 and its variant polymorphisms on host responses and viral pathogenesis, Cell Host & Microbe (2023), https://doi.org/10.1016/j.chom.2023.08.003

Continued

REAGENT or RESOURCE	SOURCE	IDENTIFIER
NFKB1-AlexaFluor 647-conjugated RNA probe	ThermoFisher	Cat#VA6-16931-VC
NUAK2-AlexaFluor 647-conjugated RNA probe	ThermoFisher	Cat#VA6-3180987-VCP
Recombinant DNA		
pCAGGS plasmid	Dr. Adolfo García-Sastre's laboratory stock	N/A
pCAGGS-SARS-CoV-2 ORF6-HA	Miorin et al.[8]	N/A
pCAGGS-SARS-CoV-2 ORF6(M58R)-HA	Miorin et al.[8]	N/A
pCAGGS-SARS-CoV-2 ORF6(D61L)-HA	This paper	N/A
pCAGGS-FLAG-RIG-I 2CARD	Escalante et al.[49]	N/A
pCAGGS-IRF3-GFP	Escalante et al.[49]	N/A
pCAGGS-HCV NS3/4A-HA	Sanchez-Aparicio et al.[50]	N/A
pCAGGS-STAT1-GFP	Ashour et al.[51]	N/A
pCAGGS-STAT2-RFP	Ashour et al.[51]	N/A
pCAGGS-HA-TRIM9	Versteeg et al.[52]	N/A
pRL-TK (constitutive Renilla luciferase)	Promega	Cat#: E2241
ISG54-firefly (ISRE promoter-controlled Firefly luciferase)	Versteeg et al.[52]	N/A
p55C1-Luc (3xIRF3 responsive promoter-controlled Firefly luciferase)	Manganaro et al.[53]	N/A
pNFkB-Luc(NFKB responsive promoter-controlled Firefly luciferase)	Versteeg et al.[52]	N/A
pGEM-SARS-CoV-2(11984-13321)	This paper	N/A
Software and algorithms		
GraphPad Prism	Graphpad software	https://www.graphpad.com/features
Fiji image analysis software	N/A	https://imagej.nih.gov/ij/
R language	N/A	N/A
Spectronaut version 15.6.211220.50606 (Rubin)	Biognosys	https://biognosys.com/software/spectronaut/
R package artMS (version 1.8.1).	N/A	http://artms.org
Maxquant (version 1.6.12)	Maxquant	https://www.maxquant.org
Lasergene	DNAstar	N/A
MinKNOW	Oxford Nanopore	https://nanoporetech.com/products/minion
HALO histopathology analysis software	Indica Labs	https://indicalab.com/halo/

RESOURCE AVAILABILITY

Lead contact

Further information and requests for resources and regents may be directed to and will be fulfilled by the lead contact Dr. Adolfo García-Sastre

Materials availability

All unique reagents generated in this study are available from the lead contact without restriction, except for recombinant SARS-CoV-2 viruses, available from Dr. Luis Martinez-Sobrido with a completed MTA.

Data and code availability

- The mass spectrometry abundance proteomics and phosphoproteomics data have been deposited to the ProteomeXchange Consortium via the PRIDE partner repository[54] and are publicly available as of the date of publication (PXD036821). Bulk RNA-Seq data and corresponding SARS-CoV-2 sgmRNA processed data files, along with complete details to generate processed sgmRNA count data, are accessible at the NCBI Gene Expression Omnibus (GEO), accession number GSE215433.
- This paper does not report original code
- Any additional information required to reanalyze the data reported in this paper is available from the lead contact upon request.

Please cite this article in press as: Kehrer et al., Impact of SARS-CoV-2 ORF6 and its variant polymorphisms on host responses and viral pathogenesis, Cell Host & Microbe (2023), https://doi.org/10.1016/j.chom.2023.08.003

EXPERIMENTAL MODEL AND SUBJECT DETAILS

Ethics Statement

All SARS-CoV-2 *in vitro* infections were performed under BSL3 containment in accordance with the biosafety protocols developed by the Icahn School of Medicine at Mount Sinai (ISMMS). All *in vivo* infections were carried out in a CDC/USDA-approved BSL-3 facility at ISMMS CCMS. Experimental protocols were approved by the Institutional Animal Care and Use Committee at Icahn School of Medicine at Mount Sinai.

Cell lines

Vero E6 (ATCC, CRL-1586) and TMPRSS2-Vero E6 (BPS Bioscience Cat# 78081) were maintained in Dulbecco's modified Eagle's medium (Corning) supplemented with 10% fetal bovine serum (Peak Serum), 1% non-essential amino acids (Gibco), 1% HEPES (Gibco) and 1% penicillin/streptomycin (Corning) at 37 °C and 5% CO2. HEK293T (ATCC, CRL-3216), A549-ACE2 (previously described in Miorin et al.[47] and Daniloski et al.[55]), L929 (ATCC, CCL-1), and BHK-21 (ATCC, CCL-10) were maintained in Dulbecco's modified Eagle's medium (Corning) supplemented with 10% fetal bovine serum (Peak Serum) and penicillin/streptomycin (Corning) at 37 °C and 5% CO2. All cell lines used in this study were regularly screened for Mycoplasma contamination, using the Universal Mycoplasma Detection Kit (ATCC, 30-1012K).

Viruses and infections

Virus infections were performed using SARS-CoV-2, isolate USA-WA1/2020 (BEI Resources NR-52281), SARS-CoV-2 BA.1 (isolate: PV44488), SARS-CoV-2 BA.2 (isolate: PV56107), SARS-CoV-2 BA.4 (BEI Resources NR-56803), and SARS-CoV-2 BA.5 (isolate: PV58128). Additionally, four recombinant SARS-CoV-2 (rSARS-CoV-2) viruses, based on the USA-WA1/2020 reference sequence were used. The rSARS-CoV-2 WT and rSARS-CoV-2 ΔORF6 have been previously described.[26] A recombinant virus with a single amino acid mutation in ORF6 at position 58, rSARS-CoV-2 ORF6^{M58R}, was generated for this study. rSARS-CoV-2 ORF6^{M58R}, was generated using the same bacterial artificial chromosome (BAC)-based SARS-CoV-2 reverse genetic system previously described.[25] Briefly, two oligonucleotides were used to introduce the M58R coding change into fragment 1 by site-directed mutagenesis (rSARS-CoV-2 ORF6^{M58R}-forward and rSARS-CoV-2 ORF6^{M58R}-reverse). The region in the wild-type BAC between the unique restriction sites of BamHI and RsrII was replaced by the one from fragment 1 containing the M58R mutation, and the newly generated BAC was used to produce the rSARS-CoV-2 ORF6^{M58R} virus according to the protocol described previously.[27] A recombinant virus with STOP codon mutations in ORF6 at position 1,2, and 19, rSARS-CoV-2 ORF6^{STOP}, was generated for this study using the same reverse genetic system previously described. Briefly, two oligonucleotides were used to introduce three STOP codons (ATG to TAA) into fragment 1 by site-directed mutagenesis (rSARS-CoV-2 ORF6^{STOP}-forward and rSARS-CoV-2 ORF6^{STOP}-reverse). As described above, the region in the wild-type BAC between the unique restriction sites of BamHI and RsrII was replaced by the one from fragment 1 containing the STOP mutations. All viral stocks were grown in Vero E6 cells (except for Omicron subvariants, which were grown in Vero-TMPRSS2 cells) and validated by genome sequencing.[8] Sequencing was either performed using the MinION sequencer (Oxford Nanopore Technologies) or with the Nextera XT DNA Sample Preparation kit (Illumina) as described elsewhere.[56,57] Virus growth media (VGM) was used for all infections: Dulbecco's modified Eagle's medium (Corning) supplemented with 2% fetal bovine serum (Peak Serum), 1% non-essential amino acids (Gibco), 1% HEPES (Gibco) and 1% penicillin/streptomycin (Corning) at 37 °C and 5% CO2. Viral stocks for *in vivo* studies were concentrated using Amicon ultra-centrifugal filters (100 kDa MW-cutoff, Millipore).

SARS-CoV-2 infection of Syrian Golden Hamsters

For the *in vivo* infection studies, experiments were conducted in 8-week-old female Syrian Golden Hamsters (Envigo, strain: HsdHan®:AURA) of approximately 120 grams body weight. The hamsters were housed in ventilated cages with free access to food and water and environmental enrichment. Cages were situated in a BSL3 vivarium with a light-cycle of 14 hours on, 10 hours off. Hamsters were intranasally mock-infected (n=8) or infected with 5x10^5 PFU of either rSARS-CoV-2 WT or rSARS-CoV-2 ΔORF6 (n=17 per group) in a 100uL total inoculum. Virus was diluted in PBS. Ketamine (100mg/kg)/ Xylazine(5mg/kg) was used to anesthetize the animals prior to infection. After infection, animals were monitored daily for morbidity and mortality up to day 15 post-infection. Necropsies were performed at 2, 4, 6, and 15 days post-infection (dpi). Animals were anesthetized with 200 uL Ketamine/Xylazine at a dose of 100 mg/kg of ketamine and 10 mg/kg xylazine and terminally bleed. Lungs and nasal turbinates were harvested. Total lung weight was measured. The left lobe of the lung was harvested, stored in Formalin (Fisherbrand), and processed for histology. The bottom right lobe of the lung and nasal turbinates were homogenized in 750uL PBS and used for plaque assay. Matched hamsters were bled from the footpad at day 0 and day 15 post-infection and sera was isolated from whole blood by centrifugation to assess antibody titers. For the re-challenge experiment, animals were challenged with 1x10^5 PFU of SARS-CoV-2 (USA-WA1/2020) (n=4 per group) at 30 days after initial infection. Animals were monitored for morbidity and mortality for up to 6 days post-challenge (36 days after initial infection). Nasal washes were performed at day 2, 4, and 6 post challenge with 250uL of PBS for assessment of viral titers by plaque assay.

Please cite this article in press as: Kehrer et al., Impact of SARS-CoV-2 ORF6 and its variant polymorphisms on host responses and viral pathogenesis, Cell Host & Microbe (2023), https://doi.org/10.1016/j.chom.2023.08.003

SARS-CoV-2 infection of K18 human ACE2 transgenic mice

Experiments were conducted in 6- to 8-week-old female B6.Cg-Tg(K18-ACE2)2Prlmn/J mice (Jackson Laboratories). The mice were housed in ventilated cages with free access to food and water and environmental enrichment. Cages were situated in a BSL3 vivarium with a light-cycle of 14 hours on, 10 hours off. Animals were treated with either 2mg anti-mouse IFNAR-1 antibody (I-1188, Leinco Technologies) or anti-mouse IgG2a isotype control (M1411, Leinco Technologies) intraperitonially one day before infection. Mice were intranasally mock-infected or infected with $1x10^4$ PFU of either rSARS-CoV-2 WT or rSARS-CoV-2 ORF6 ^{M58R} in a 30uL total inoculum (n=6 for IgG isotype-treated and mock-infected, n=8 for rIFNAR Ab-treated and mock-infected, n=9 for rSARS-CoV-2 WT-infected groups and rSARS-CoV-2 ORF6 ^{M58R}-infected groups). Virus was diluted in PBS. Ketamine (80mg/kg)/ Xylazine(12.5mg/kg) was used intraperitoneally to anesthetize the animals prior to infection. After infection, animals were monitored daily for morbidity and mortality up to day 10 post-infection. Animals were treated with either 1mg anti-mouse IFNAR-1 antibody (MAR1-5A3 Purified *in vivo* PLATINUM functional grade, Leinco Technologies, Inc.) or anti-mouse IgG1 isotype control (Purified *in vivo* PLATINUM functional grade, Leinco Technologies, Inc.) intraperitonially on day 2 and 5 post-infection. Necropsies were performed at day 5 post-infection. Animals were euthanized with pentobarbital given intraperitoneally. Lungs, nasal turbinates and brains were harvested and processed for viral titers. Tissues were put in 1mL of PBS and homogenized 3 times at 4 M/S, centrifuged, and supernatants were processed for viral titers by plaque assay in Vero E6 cells as described below.

METHOD DETAILS

Plaque assay

Unless otherwise specified, plaque assays were performed using Vero E6 cells in 12-well format as previously described.[58] Briefly, confluent Vero E6 cells were infected with serial ten-fold dilutions of supernatants of infected cells or supernatants of homogenized tissue. Infections were performed in 12-well format for 1h at 37°C and 5% CO2 using an inoculum of 200uL, rocking plates every 10–15 min. An overlay of MEM with penicillin/streptomycin (Corning), L-Glutamine (Gibco), HEPES (Gibco), BSA (MP Biomedicals), and $NaHCO_3$ supplemented with 0.7% purified agar (Oxoid) and 2% fetal bovine serum (Peak Serum) was applied to each well. On day 3 post-infection, cells were fixed with 5% formaldehyde overnight and immuno-stained using a monoclonal anti-SARS-CoV-N antibody (1C7C7) at a 1:1,000 dilution, an anti-mouse HRP antibody (Abcam ab6823) at a 1:5,000 dilution, and TrueBlue (SeraCare) for detection. All samples were frozen at -80°C once before evaluation of viral titers.

Western Blot and immunoprecipitation

Vero E6 or A549-ACE2 cells were seeded in a 24-well format at a density of 100,000 cells/well. The next day, cells were infected with SARS-CoV-2 at the indicated MOI in viral growth media for 1 hour after which the inoculum was removed, and samples were harvested at 24 hpi. Cells were either lysed directly or stimulated with universal IFN type I (1,000 U/mL) for 45 min before lysis. SARS-CoV-2-infected cells were lysed in radio-immunoprecipitation assay (RIPA) buffer (Sigma-Aldrich) supplemented with 1% sodium dodecyl sulfate, cOmplete protease inhibitor mixture (Roche), and Halt phosphatase inhibitor mixture (Thermo Fisher Scientific) before boiling for virus inactivation. Lysates were normalized for protein concentration using a BCA protein assay (Pierce), supplement with 4X Laemmli sample buffer (Bio-Rad Laboratories), boiled for 10 min, and loaded into 4-20% gradient gels (Bio-Rad Laboratories). Gels were transferred onto polyvinylidene fluoride (PVDF) membranes (Bio-Rad Laboratories) using the Trans-Blot Turbo Transfer System (Bio-Rad Laboratories). Membranes were blocked in Tris-buffered saline with 0.1% Tween 20 detergent (TBS-T) containing 5% nonfat dry milk. Primary antibodies were diluted 1:1,000 in TBS-T containing 3% bovine serum albumin. Secondary horseradish peroxidase-conjugated antibodies were diluted 1:10,000 in TBS-T containing 3% nonfat dry milk. For immunoprecipitation of endogenous Nup98, A549-ACE2 cells were seeded in a 10-cm dish format. Cells were infected with indicated viruses at MOI 2 for 24h. Next, cells were processed as described before.[11] In brief, cells were lysed in lysis buffer (50 mM Tris (pH 7.5), 150 mM NaCl, 1% IGEPAL CA-630, 0.1 mM Na3VO4, 1 mM NaF, 1 mM DTT, 1 mM EDTA, 1 mM PMSF, 1×cOmplete protease inhibitor mixture and 10% glycerol) for 30 min on ice then incubated at 65°C for 30min to inactivate virus. Inactivated samples were sonicated and then cleared by centrifugation. Lysates were incubated with 10 ug of anti-Nup98 antibody or an irrelevant isotype control (IgG DA1E, Cell signaling) overnight and subsequently incubated with protein G-beads for 2h. Beads were washed and protein was eluted by addition of a 2x sample buffer. Samples were processed following the western blot protocol described above. For immunoprecipitation of ORF6-HA, 500,000 HEK 293T cells were transfected with 1 ug of indicated constructs. At 24 hours post-transfection, cells were lysed in RIPA buffer, cleared by centrifugation, and incubated with EZview Red Anti-HA Affinity Gel beads (Millipore Sigma) at 4 C overnight while shaking. Next, beads were washed for five-times for 5 mins in RIPA buffer at 4 C while shaking before elution of bound proteins by boiling the beads in 2x Laemmli buffer for 10 min at 95 C.

SARS-CoV-2 infection of HTBE cultures (EpiAirway AIR-100 tissues)

EpiAirway AIR-100 tissue inserts were transferred to 12-well plates containing AIR-100 maintenance medium (#AIR-100-MM, Mattek) per the manufacturer's instructions. The next day, tissues were washed with 250uL TEER buffer (#TEER-BUFFER, Mattek) for 15min at 37 °C and 5% CO_2 on the apical side. TEER buffer was removed and tissues were mock-infected or infected with 10^5 PFU on the apical side of either rSARS-CoV-2 WT, rSARS-CoV-2 ΔORF6 or rSARS-CoV-2 ORF6 M58R for 2h. Infections were performed in 100uL of VGM at 37 °C and 5% CO_2. Inoculum was removed 2h post-infection. At 24, 48, and 72 h post-infection, a wash of

Please cite this article in press as: Kehrer et al., Impact of SARS-CoV-2 ORF6 and its variant polymorphisms on host responses and viral pathogenesis, Cell Host & Microbe (2023), https://doi.org/10.1016/j.chom.2023.08.003

the apical side was performed using 150uL TEER buffer for 15min at 37 °C and 5% CO_2. Apical washes were stored at -80°C before evaluation of viral titers. Titers were quantified by plaque assay in TMPRSS2-Vero E6 cells as described above.

Luciferase Assay

For luciferase assays, HEK293T cells were seeded in a 24-well format at a density of 100,000 cells/well. The next day, cells were transiently transfected with pRL-TK and either the IRF3 responsive p55C1 promoter (p55C1-Luc) or the NFkB-Luc vector along with the indicated plasmids. For NFkB reporter experiments, cells were treated overnight with human TNF-alpha (25ng/ml) at 24 hours after transient transfection. For the IRF3 reporter experiments, cells were co-transfected with RIG-I-2CARD (5 ng) and lysed at 24 hours after transfection using Passive Lysis Buffer (Promega). Samples were processed and luciferase activity was measured using the Dual-Luciferase Assay System (Promega) according to the manufacturer's instructions. Firefly luciferase values were normalized to Renilla luciferase values, and the induction was calculated as fold over unstimulated vector control condition.

Confocal Microscopy

Vero E6, A549-ACE2, HEK293T, or BHK-21 cells were seeded into 24-well glass bottom plates (MatTek) at a low density the day before infection or transfection. For infection experiments, cells were infected at the indicated MOI for 24 hours, then fixed with 5% methanol-free formaldehyde or treated with universal IFN-I at 1,000 U/mL (PBL) for 45 min before fixation. Quantification was done by comparing nuclear translocation of STAT, IRF3, p65 in infected cells (N-positive cells) compared to mock-infected cells. For overexpression experiments, indicated plasmids were transfected using LT-1 Reagent (Mirus) and cells were then fixed with 5% methanol-free formaldehyde or treated with IFN or TNF-alpha before fixation. IFN treatments were performed for 45 min using universal IFN-I at 1,000 U/mL (PBL). TNF-alpha treatments were performed for 45 min using 25 ng/ml of human TNF-alpha (Thermo Fisher). Quantification was done by comparing nuclear translocation of indicated proteins in ORF6-co-transfected cells (HA-positive cells) compared to mock-transfected cells. Cells were permeabilized with 0.1% Triton X in phosphate-buffered saline (PBS) and stained as previously described.[8] Confocal laser scanning microscopy was performed with a Zeiss LSM880 confocal laser scanning microscope (Carl Zeiss Microimaging) fitted with a Plan Apochromat 63×/1.4 or 40×/1.4 oil objective, or with a 20x/1.4 objective. Images were analyzed with Fiji software (https://fiji.sc/). All scale bars indicate a length of 20 μm.

Flow Cytometry

A549-ACE2 cells were seeded in 24-well format at a density of 150,000 cells/well. The next day, cells were infected at indicated MOI for 24 hours. Cells were detached with PBS supplemented with 10 mM EDTA (Gibco) and fixed with 5% formaldehyde. Cells were permeabilized and washed with Perm/Wash buffer (BD), and then stained with monoclonal anti-SARS-N antibody conjugated to AlexaFluor488 (Invitrogen) for 1 hour. Cells were washed with and resuspended in PBS supplemented with 2% BSA, 2.5 mM EDTA and subsequently subjected to cytometry using a Gallios cytometer (Beckman). 10,000 cells were acquired for each condition. Single cells were gated and the percentage of N-positive cells was used to determine infection rates for rSARS-CoV-2 WT, ΔORF6, and $ORF6^{M58R}$ viruses. Mean fluorescence intensity of N-positive cells was also measured for the N-positive cells in each condition.

Nuclear-cytosolic fractionation

A549-ACE2 cells were infected at the indicated MOI for 24 hours and subsequently washed with PBS and detached with 10mM EDTA (Gibco). After washing with PBS, cells were resuspended in one volume buffer A (15 mM Tris-HCl pH 8 (Boston Bioproducts), 15 mM NaCl (Corning), 60 mM KCl (Sigma-Aldrich), 1 mM EDTA pH 8 (Invitrogen), 0.5 mM EGTA pH 8 (BioWorld), Spermidine 0.5 mM (Sigma-Aldrich), RNasin 100 U/mL (Thermo-Fisher) and cell membranes were lysed by addition of one volume of buffer A, supplemented with 0.8% NonIdent 40 (US Biological Life Sciences) for 5 min. Cytoplasmic supernatant was separated from nuclei by centrifugation, before washing the nuclei with PBS. Next, nuclei were resuspended in one volume of RLN buffer (50 mM Tris-HCl pH 8, 140 mM NaCl, 1.5 mM Mg2Cl (Sigma-Aldrich), 10 mM EDTA pH 8, RNasin 100 U/mL, 0.8% NonIdent 40) and then lysed by addition of one volume of RLN buffer, supplemented with 0.8% NonIdent 40, for 5 minutes. Debris was removed by centrifugation and cytoplasmic and nuclear fractions were lysed in TriZol reagent (Ambion). 500ng of isolated RNA were reverse transcribed using the High-Capacity cDNA Reverse Transcription Kit (Applied Biosystems) according to manufacturer's instructions. Quantitative real-time PCR was performed using TaqMan Universal Master Mix II with UNG (Applied Biosystems) according to the manufacturer's instructions. Cycling program with 50 amplification cycles was designed according to the manufacturer's instructions. The following TaqMan (ThermoFisher) primer/probe mixes were used: MALAT-1 (Hs00273907_s1), NUAK2 (Hs00388292_m1), NFKB 1 (Hs00765730_m1), CXCL3 (Hs00171061_m1), IRF1 (Hs00971965_m1), and GAPDH (Hs02786624_g1). Transcripts from each fraction were normalized to a housekeeping gene of the respective compartment (GAPDH for cytosolic fraction, MALAT-1 for nuclear fraction). After normalization, nuclear-cytosolic ratios were calculated for each sample.

SARS-CoV-2 RT-qPCR

To generate SARS-CoV-2 gRNA standards for quantification of copy numbers, the sequence encoding the section from position 11984 to 13321 in the viral genome, that is covered by the primers used for gRNA amplification (see key resources table), was cloned by PCR amplification of viral cDNA into a pGEM vector under control of a T7 promoter using pGEM-T Easy Vector System (Promega). RNA standards were subsequently generated by *in vitro* transcription using the mMESSAGE mMACHINE™ T7 Transcription Kit (Invitrogen) according to the manufacturer's instructions. For quantification of viral genome copies during infection, A549-ACE2 were

Please cite this article in press as: Kehrer et al., Impact of SARS-CoV-2 ORF6 and its variant polymorphisms on host responses and viral pathogenesis, Cell Host & Microbe (2023), https://doi.org/10.1016/j.chom.2023.08.003

mock-infected or infected at indicated MOI for 24h before lysis in Trizol (Invitrogen). RNA was isolated using DirectZol RNA kit (Zymo Research) or miRNeasy kit (Qiagen) according to the manufacturer's instructions. Isolated RNA or serial ten-fold dilutions of RNA standards for the ORF1ab amplicon (ranging from 2.25x10^6 to 250 copies/rxn) were reverse transcribed using the Takara Prime Script RT kit (Takara) using poly(A) primers according to manufacturer's instructions. TaqMan Universal Master Mix II with UNG (Applied Biosystems) was used for the PCR according to the manufacturer's instructions. Cycling program with 40 amplification cycles was also designed according to the manufacturer's instructions. GAPDH was used as endogenous gene control and was amplified using the commercial primer/probe set hs02786624_g1 (Applied biosystems). Primers for viral gene amplification were used at 500 nM each, while probes were used at concentration of 250nM. Primer/probe sets were previously described (see STAR Methods table).[48] For quantification of gRNA and sgRNAs, The LightCycler® 480 SYBR Green I Master mix (Roche) was used according to the manufacturer's instructions. Cycling program with 50 amplification cycles was also designed according to the manufacturer's instructions. Primers were used at a final concentration of 1 uM. A leader specific forward primer was used for all reactions and a gene specific reverse primer was designed for each target (see STAR Methods table). Results were adjusted for primer efficiency as described previously.[59]

Immunolabeling with fluorescent in situ hybridization (Immuno-FISH)

HEK293T cells were seeded on glass-slides at a low density and transfected with the indicated plasmids for 24h. Cells were fixed, stained, and processed as described before.[11] Confocal laser scanning microscopy was performed with a Zeiss LSM880 confocal laser scanning microscope (Carl Zeiss Microimaging) fitted with a Plan Apochromat 63×/1.4 or 40×/1.4 oil objective. Analysis of the nuclear/cytoplasmic ratio of poly(A) RNA signal was performed as described elsewhere.[60]

Immunolabeling with single-molecule RNA-FISH (smRNA-FISH)

A549-ACE2 cells were seeded on glass cover slips (no 1.5) at a low density. 24 h after seeding, cells were infected with indicated viruses at an MOI of 0.25 for 24 hours before fixation and processing for smRNA-FISH using the ViewRNA Cell Plus Assay Kit (Invitrogen). Probes for transcript detection were purchased from ThermoFisher: NFKB1 (VA6-16931-VC, Alexa 647-conjugated), NUAK2 (VA6-3180987-VCP, Alexa 647-conjugated). Staining was performed according to manufacturer's instructions with the exception that probe hybridization and signal amplification steps during the staining procedure were lengthened by 30 min. Anti-SARS N antibody (1C7C7) was used at a dilution of 1:300 and all probes were used at a dilution of 1:100. Coverslips were mounted onto glass slides using Prolong Gold Antifade Mountant with DNA Stain DAPI (Invitrogen). Confocal laser scanning microscopy was performed with a Zeiss LSM880 confocal laser scanning microscope (Carl Zeiss Microimaging) fitted with a Plan Apochromat 63×/1.4 oil objective to acquire 0.5 μm optical z-sections spanning a cell volume. Imaris-assisted image analysis was used to quantify images. The Imaris software package Cells module (Bitplane, Version 9.8.2) was used to identify and create a conventional 2-dimensional maximum intensity image of the nucleus (DAPI-stained chromatin), SARS-CoV-2 N and ViewRNA-ISH signal. First, nuclei (DAPI) were segmented using an automated threshold (based on the intensity distribution histogram) in 405 nm laser line. Identified nuclei populations were filtered to remove large nuclei aggregates (upper nuclei volume threshold and lower threshold to manual remove fragments of nuclei at the edges of the stack) using the Imaris surface tool. Next, SARS-CoV-2 N expression (used as marker protein for infected cells) and ViewRNA-ISH signal for selected mRNA were identified in 488 nm laser line using Imaris surface tool and 647 nm laser line using the Imaris spot tool, respectively. Cell segmentation was done in manual drawing mode at 1 mm vertex spacing. The seed spot size used was 0.2-0.7 mm. For objective mRNA foci center identification, automatic thresholds were used to filter raw spot quality. After identification of all mRNA spots in the cell, the nuclear mRNA spots were segmented, setting the spot filter function to the ''shortest distance to Nucleus'' upper-threshold to 0 and turning the lower-threshold off.

Mass spectrometry (MS)

Cell lysis and digestion for proteomics

At the indicated time after infection A549-ACE2 cells were washed three times in ice cold 1x PBS. Next, cells were lysed in 500uL/well of 6M guanidine hydrochloride (Sigma) in 100mM Tris-HCl (pH 8.0) (Boston Bioproducts) and scraped with a cell spatula for complete collection of the sample. Samples were then boiled for 5 minutes at 95°C to inactivate proteases, phosphatases and the virus. Samples were frozen at -80°C until further processing. Samples were sonicated with a probe sonicator three times for 10 seconds at 20% amplitude. Insoluble material was pelleted by spinning samples at 13,000rpm for 10 minutes. Supernatant was transferred to a new protein lo-bind tube and protein was quantified using a Bradford assay. Samples were processed for reduction and alkylation using a 1:10 sample volume of tris-(2-carboxyethyl) (TCEP) (10mM final) and 2-chloroacetamide (4.4mM final) for 5 minutes at 45°C with shaking. Prior to protein digestion, the 6M guanidine hydrochloride was diluted 1:6 with 100mM Tris-HCl pH8 to increase the activity of trypsin and LysC proteolytic enzymes, which were subsequently added at a 1:75 (wt/wt) enzyme-substrate ratio and placed in a 37°C water bath for 16-20 hours. Following digestion, 10% trifluoroacetic acid (TFA) was added to each sample to a final pH ~2. Samples were desalted under vacuum using 50mg Sep Pak tC18 cartridges (Waters). Each cartridge was activated with 1 mL 80% acetonitrile (ACN)/0.1% TFA, then equilibrated with 3 × 1 mL of 0.1% TFA. Following sample loading, cartridges were washed with 4 × 1 mL of 0.1% TFA, and samples were eluted with 2 × 0.4 mL 50% ACN/0.25% formic acid (FA). Approximately 60μg of each sample was kept for protein abundance measurements, and the remainder was used for phosphopeptide enrichment. Samples were dried by vacuum centrifugation. Thus, the same original sample was used for abundance proteomics and phosphoproteomics analysis.

Phospho-peptide enrichment for phospho-proteomics

IMAC beads (Ni-NTA from Qiagen) were prepared by washing 3x with HPLC water, incubating for 30 minutes with 50mM EDTA pH 8.0 to strip the Ni, washing 3x with HPLC water, incubating with 50mM FeCl3 dissolved in 10% TFA for 30 minutes at room temperature with shaking, washing 3x with and resuspending in 0.1% TFA in 80% acetonitrile. Peptides were enriched for phosphorylated peptides using a King Flisher Flex. For a detailed protocol, please contact the authors. Phosphorylated peptides were found to make up more than 90% of every sample, indicating high quality enrichment.

MS acquisition and data preprocessing for abundance proteomics

Digested samples were analyzed on an Orbitrap Fusion Lumos Tribrid mass spectrometry system (Thermo Fisher Scientific) equipped with an Easy nLC 1200 ultra-high pressure liquid chromatography system (Thermo Fisher Scientific) interfaced via a Nanospray Flex nanoelectrospray source. For all analyses, samples were injected on a C18 nano flow column (15 cm x 150 μm ID packed with PepSep1.9 μm particles). Mobile phase A consisted of 0.1% FA, and mobile phase B consisted of 0.1% FA/80% ACN. Peptides were separated by a linear gradient from 3% to 30% mobile phase B over 90 minutes, 30% to 38% B over 8 minutes, 38% to 88% B over 2 minutes, then held at 88% B for 10 minutes at a flow rate of 600 nL/minute (total of 110 minutes). Analytical columns were equilibrated with 6 μL of mobile phase A. Data was acquired using data independent acquisition (DIA) mode with the following parameters. A cycle consisted of a full FTMS scan at 120,000 resolving power over a scan range of 300-1400 m/z, a normalized AGC target of 100%, an RF lens setting of 30%, and a maximum injection time of 50 ms. DIA scan windows were variable, with 20 16m/z windows from 358-643m/z, 8 18m/z windows from 659-795m/z, 6 20m/z windows from 813-908m/z, 4 25m/z windows from 929.5-977.5m/z, 1 35m/z window at 1006.5m/z, 1 50m/z window at 1048m/z, and one 78m/z window at 1111m/z. Cycle time was 3 seconds. Loop control was set to 3. Raw mass spectrometry data from each run was analyzed the directDIA Analysis function in Spectronaut version 15.6.211220.50606 (Rubin) by Biognosys (no spectral library used). Data was searched against proteomics for Homo sapiens (downloaded February 28, 2020) and 29 SARS-CoV-2 protein sequences translated from genomic sequence downloaded from GISAID (accession EPI_ISL_406596, downloaded March 5, 2020). Data were searched using the default BGS settings, variable modification of methionine oxidation, static modification of carbamidomethyl cysteine, and filtering to a final 1% false discovery rate (FDR) at the peptide, peptide spectrum match (PSM), and protein level. Between run normalization was disabled and performed later using artMS (see below). On average, 5 data points per peak in MS1 and MS2 were captured per sample.

MS acquisition and data preprocessing for phosphoproteomics

Phospho-enriched samples were analyzed on a Q Exactive Plus Quadrupole-Orbitrap mass spectrometry system (Thermo Fisher Scientific) equipped with an Easy nLC 1200 ultra-high pressure liquid chromatography system (Thermo Fisher Scientific) interfaced via a Nanospray Flex nanoelectrospray source. For all analyses, samples were injected on a C18 reverse phase column (25 cm x 75 μm packed with ReprosilPur 1.9 μm particles). Mobile phase A consisted of 0.1% FA, and mobile phase B consisted of 0.1% FA/80% ACN. Peptides were separated by a linear gradient from 2% to 4% for 1 minute, 4% to 24% for 56 minutes, 24% to 38% for 19 minutes, 38% to 90% for 3 minutes, held at 90% for 8 minutes, then decreased from 90% to 2% for 1 minute and held at 2% for 2 minutes at a flow rate of 300nL/minute (total of 90 minutes). Analytical columns were equilibrated with 6 μL of mobile phase A. Data was acquired using data dependent acquisition (DDA) mode, acquired over a range of 300-1500 m/z in the Orbitrap at 70,000 resolving power with a normalized AGC target of 300%, an RF lens setting of 40%, and a maximum ion injection time of 60 ms. Dynamic exclusion was set to 60 seconds, with a 10 ppm exclusion width setting. Peptides with charge states 2-6 were selected for MS/MS interrogation using higher energy collisional dissociation (HCD), with 20 MS/MS scans per cycle. MS/MS scans were analyzed in the Orbitrap using isolation width of 1.3 m/z, normalized HCD collision energy of 30%, normalized AGC of 200% at a resolving power of 30,000 with a 54 ms maximum ion injection time. Raw mass spectrometry data from each run was analyzed using Maxquant (version 1.6.12). Data was searched against proteomics for Homo sapiens (downloaded February 28, 2020) and 29 SARS-CoV-2 protein sequences translated from genomic sequence downloaded from GISAID (accession EPI_ISL_406596, downloaded March 5, 2020). Data were searched using default settings, variable modification of methionine oxidation and phosphorylation (STY), static modification of carbamidomethyl cysteine, and filtering to a final 1% false discovery rate (FDR) at the peptide, peptide spectrum match (PSM), and protein level.

MS quantitative comparison analysis for abundance and phospho-proteomics

Quantitative analysis was performed in the R statistical programming language (version 4.0.2, 2020-06-22). Initial quality control analyses, including inter-run clustering, correlations, principal components analysis (PCA), peptide and protein counts and intensities were completed with the R package artMS (version 1.8.1). Based on obvious outliers in intensities, correlations, and clusterings in PCA analysis, 1 run was discarded from the protein abundance dataset (d6 [ΔORF6] replicate 2); no runs were discarded from the phosphorylation dataset. Statistical analysis of phosphorylation and protein abundance changes between wild-type (WT), d6 (ΔORF6), and M58R (ORF6M58R) infected samples were calculated using peptide ion fragment data output from Spectronaut and processed using artMS. Specifically, quantification of phosphorylation peptide ions were processed using artMS as a wrapper around MSstats, via functions artMS::doSiteConversion and artMS::artmsQuantification with default settings. All peptides containing the same set of phosphorylated sites (but different elution times or charge states) were grouped and quantified together into phosphorylation site groups. For both phosphopeptide and protein abundance MSstats pipelines, MSstats performs normalization by median equalization, imputation of missing values and median smoothing (Tukey's Median Polish) to combine intensities for multiple peptide ions or fragments into a single intensity for their protein or phosphorylation site group, and statistical tests of differences in intensity between infected and control time points. When not explicitly indicated, we used defaults for MSstats for adjusted p-values, even in cases of N = 2. By default, MSstats uses Student's t-test for p-value calculation and Benjamini-Hochberg method

of FDR estimation to adjust p-values. After quality control data filtering, principal components analysis (PCA) and Pearson's correlation confirmed strong correlation between biological replicates, time points, and conditions (except for the one run that was discarded).

Viral protein quantification

Median normalized peptide feature (peptides with unique charge states and elution times) intensities (on a linear scale) were refined to the subset that mapped to SARS-CoV-2 protein sequences as defined by MaxQuant (see above). Peptides found in the same biological replicate (i.e. due to different elution times, charge states, or modifications, for example) were averaged at the intensity level. Next, we selected the subset of peptides that were consistently detected in all biological replicates across all conditions (allowing no missing values), isolating the set of peptides that were consistently detected across all runs and thus possessing the best comparative potential. Isolating to this set of peptides, we summed all peptides mapping to each viral protein within each sample, which produced a final intensity value per viral protein, per sample. These resulting protein intensities were averaged across biological replicates and standard errors were calculated for each condition. To calculate the ratios, averaged intensities from each condition were divided (e.g. ΔORF6/WT). The standard error (SE) of the ratios was calculated as (A/B) * sqrt($(se.A/A)^2$ + $(se.B/B)^2$).

Bulk RNA Sequencing

Samples for bulk RNA sequencing were lysed in Trizol Reagent and total RNA was extracted using the miRNeasy mini kit (Qiagen) per the manufacturer's instructions. DNAse treatment was performed on isolated RNA using the RNA Clean and Concentrator Kit (Zymo). Total RNA was examined for quantity and quality using the TapeStation (Agilent) and Quant-It RNA (ThermoFisher) systems. RNA samples with sufficient material (10 pg–10 ng) were passed to whole-transcriptome library preparation using the SMART-Seq v4 PLUS Kit (Takara Bio) following the manufacturer's instructions. Briefly, total RNA inputs were normalized to 10ng in 10.5 μl going into preparation. 3' ends of cDNA were then adenylated prior to ligation with adapters utilizing unique dual indices (96 UDIs) to barcode samples to allow for efficient pooling and high throughput sequencing. Libraries were enriched with PCR, with all samples undergoing 14 cycles of amplification prior to purification and pooling for sequencing. Bulk RNA sequencing was conducted on dual index libraries using a 300cycle Mid Output kit on an Illumina NextSeq 500 with standaer read configurations for R1, i7 index, i5 index, and R2:150, 8,8,150. Libraries were pooled and sequenced in two independent runs at 1.5 and 1.7pM loading concentrations. No PhiX was included in the loading library. Raw BCL files were converted to fastq files using bcl2fastq/2.20.0 (Illumina, Inc). For quantification of SARS-CoV-2 sgRNA and gRNA expression, the periscope/0.1.2 package was used with the technology argument set to "illumina"[61]. Finally, sgRNA reads per total mapped reads were calculated.

Immunohistochemistry (IHC)

Multiplex fluorescent immunohistochemistry

A Ventana Discovery Ultra (Roche, Basel, Switzerland) tissue autostainer was used for brightfield and multiplex fluorescent immunohistochemistry (fmIHC). In brief tyramide signaling amplification (TSA) was used in an iterative approach to covalently bind Opal fluorophores (Akoya Bioscience, Marlborough, MA) to tyrosine residues in tissue, with subsequent heat stripping of primary-secondary antibody complexes until all antibodies were developed. Lungs from infected (positive controls) and uninfected (negative controls) hamsters were used as controls for assay optimizing. In total two monoplex 3,3′-Diaminobenzidine (DAB) chromogenic assays (Ki67 and SARS-CoV-2 Spike) and two fluorescent duplexes: STAT1 + SARS-CoV-2 Spike, and MxA + SARS-CoV-2 Spike. Specific details for the immunohistochemical assays are outlined in Table S1, with a more concise overview provided below.

Brightfield Immunohistochemistry

Antigen retrieval was conducted using a Tris based buffer-Cell Conditioning 1 (CC1)-Catalog # 950-124 (Roche). The SARS-CoV-2 spike primary antibody was of rabbit origin, and thus developed with a secondary goat anti-rabbit HRP-polymer antibody (Vector Laboratories, Burlingame, CA) for 20min at 37C. The Ki67 primary was of mouse origin, so a goat anti-mouse HRP-polymer antibody (Vector Laboratories) was utilized. Brightfield slides utilized A ChromoMap DAB (3,3′-Diaminobenzidine) Kit-Catalog #760-159 (Roche) to form a brown precipitate at the site of primary-secondary antibody complexes containing HRP. Slides were counterstained with hematoxylin and mounted.

Fluorescent Immunohistochemisty

Antigen retrieval was conducted using a Tris based buffer-CC1 (Roche). The SARS-CoV-2 Spike and Phospho-STAT1 primary antibodies were of rabbit origin, and thus developed with a secondary goat anti-rabbit HRP-polymer antibody (Vector Laboratories) for 20min at 37C. The MxA primary was of mouse origin, so a goat anti-mouse HRP-polymer antibody (Vector Laboratories) was utilized. All Opal TSA-conjugated fluorophore reactions took place for 20 minutes. Fluorescent slides were counterstained with spectral DAPI (Akoya Biosciences) for 16 minutes before being mounted with ProLong gold antifade (ThermoFischer).

Multispectral microscopy

Fluorescently labeled slides were imaged using a Vectra Polaris TM Quantitative Pathology Imaging System (Akoya Biosciences). Exposures for all Opal dyes on the Vectra were set based upon regions of interest with strong signal intensities to minimize exposure times and maximize the specificity of signal detected.

Digitalization and linear unmixing of multiplex fluorescent immunohistochemistry

Whole slide images were segmented into smaller QPTIFFs, uploaded into Inform software version 2.4.9 (Akoya Biosciences), unmixed using spectral libraries affiliated with each respective opal fluorophore including removal of autofluorescence, then fused together as a single whole slide image in HALO (Indica Labs, Inc., Corrales, NM).

Please cite this article in press as: Kehrer et al., Impact of SARS-CoV-2 ORF6 and its variant polymorphisms on host responses and viral pathogenesis, Cell Host & Microbe (2023), https://doi.org/10.1016/j.chom.2023.08.003

Quantitative analysis of multiplex fluorescent immunohistochemistry

View settings were adjusted to allow for optimal visibility of immunomarkers and to reduce background signal by setting threshold gates on minimum signal intensities. Bronchioles, interstitium, and airways were classified using the tissue random forest tissue classifier module in HALO (Indica Labs), which was developed by annotating each tissue type via manual annotations. Separate layers for interstitium, bronchioles, and the whole lung were generated from the classifier, allowing algorithms to be ran on each layer for specific anatomical compartment analysis. These annotations were extensively examined for any errors by the machine-learning classifier and manually excised as necessary. For quantifying the area of the slide that contained SARS-CoV2 Spike, an algorithm called the HALO (Indica Labs) Area Quantification (AQ) module (v2.1.11) was created and finetuned to quantify the immunoreactivity for the Spike protein based on color and stain intensity. This algorithm outputted the % of total area displaying immunoreactivity across the annotated whole slide scan in micrometers squared (μm^2). For quantifying the absolute number and overall percentage of cells expressing MxA we utilized the Halo (Indica Labs) HighPlex (HP) phenotyping modules (v4.0.4). In brief, this algorithm was used to first segment all cells within the annotated lung sections using DAPI counterstain. Detection threshold and nucleus geometry were defined until segmentation appeared accurate. Next, minimum nucleus, cytoplasm and membrane thresholds were set for each fluorophore to detect low and high expression within each of the segmented cells. Parameters were set using the real-time tuning mechanism that was tailored for each individual sample based on signal intensity. Phenotypes of infected MxA+, uninfected MxA+, infected MxA-, and uninfected MxA- cells were determined by selecting inclusion and exclusion parameters as follows respectively: MxA+S+, MxA+S-, MxA-S+, and MxA-S-. For quantifying the absolute number and overall percentage of Phospho-STAT1-expressing cells with SARS-CoV-2 infection, we utilized the Halo (Indica Labs) HighPlex phenotyping modules (v4.0.4). For determining cellular location of Phospho-STAT1 in infected cells, two algorithms were made. One captured the total number of infected cells expressing Phospho-STAT1 in the cytoplasm or nucleus, and the other determined the number of infected cells expressing STAT1 in the nucleus only. HALO does not output specific cellular location counts of defined phenotypes, so two algorithms were necessary to determine cellular location within cells with more than one marker. By subtracting the number of nuclear-expressing Phospho-STAT1+ infected cells from the total Phospho-STAT1+ infected cells, the number of cytoplasmic-only expressing cells could be determined. Phenotypes of cells were determined by selecting inclusion and exclusion parameters as follows respectively: Spike+ Phospho-STAT1+, Spike+ Phospho-STAT1-, Spike- Phospho-STAT1+, and Spike- Phospho-STAT1-. By using the outputs of these two algorithms, the number of infected cells expressing Phospho-STAT1 in the cytoplasm only could be determined. The quantitative output for the AQ and HP was exported as a.CSV.

Enzyme-Linked Immunosorbent Assay (ELISA)

96-well-microtiter plates (Thermo Fisher) were coated with 100 μL of recombinant spike protein of SARS-CoV-2 (Sino Biological, Cat. 40589-V08H4) at a concentration of 2 ug/mL at 4°C overnight. Plates were washed three times with PBS (Gibco) containing 0.1% Tween-20 (PBS-T) (Fisher Scientific) using an automatic plate washer (BioTek). After washing, plates were blocked for 1 hour at room temperature with 200 μL blocking solution per well (PBS-T with 3% milk powder (American Bio). After removing the blocking solution, serum samples were diluted to a starting concentration of 1:80, serially diluted 1:3 in PBS-T supplemented with 1% milk powder (American Bio) and incubated at room temperature for 2 h. The plates were washed three times with PBS-T and 100 uL anti-hamster IgG horseradish peroxidase antibody (HRP, abcam, #ab6892) diluted 1:10,000 in PBS-T containing 1% milk powder was added to all wells. After 1 hour of incubation at room temperature, plates were washed three times with 100 μL 3,3′,5,5′-Tetramethylbenzidine (TMB; Rockland, Cat# TMBM-100) using the plate washer and incubated at room temperature for 15 min. The reaction was stopped with 1 N sulfuric acid solution (Fisher Science). The absorbance was measured at 450 nm with a plate spectrophotometer (Synergy H1 hybrid multimode microplate reader, Biotek). Optical density (OD) for each well was calculated by subtracting the average background plus three standard deviations. Area under the curve (AUC) was computed using GraphPad Prism software.

QUANTIFICATION AND STATISTICAL ANALYSIS

Quantifications and statistics were performed as described in figure legends and methods section. Statistical significance was considered when $P \leq 0.05$. ($P \leq 0.05$ = *, $P < 0.01$ = **, $P < 0.001$ = ***, $P < 0.0001$ = ****, not significant = ns). Data were always acquired in biological triplicates and shown as average ± SD if not indicated differently.